O.I. NAKONECHNA [1], **M.M. DASHEVSKYI** [1], **O.I. BOSHKO** [2],
V.V. ZAVODYANNYI [3], **and N.N. BELYAVINA** [1]

[1] Taras Shevchenko National University of Kyiv,
  4 Glushkov Ave., UA-03022 Kyiv, Ukraine
[2] G.V. Kurdyumov Institute for Metal Physics of the N.A.S. of Ukraine,
  36 Academician Vernadsky Blvd, UA-03142 Kyiv, Ukraine
[3] Kherson State Agrarian University,
  23 Stritenska Str., UA-73006 Kherson, Ukraine

EFFECT OF CARBON NANOTUBES ON MECHANOCHEMICAL SYNTHESIS OF *d*-METAL CARBIDE NANOPOWDERS AND NANOCOMPOSITES

The nanoscale mono- (powders) and complex (compacted nanocomposites) carbides of *d*-transition metals are synthesized by mechanical alloying in a high-energy planetary ball mill from a charge containing the carbon nanotubes. The effect of multiwalled carbon nanotubes on reaction milling of the obtained materials is analyzed. The features of formation mechanism of metal carbides at the mechanical alloying are clarified. Particularly, as is shown, at the first stage of the synthesis (up to 60 min of processing of the charge in a ball mill), the amorphization of the carbon nanotubes and crushing of particles of the initial metal along the grain boundaries occurs concurrently. Then, the amorphous carbon enters into the metal lattice forming an interstitial solid solution, resulting in deformation of the metal crystal lattice. At the second stage of synthesis (from 60 to 250 minutes of processing), the process of embedding of the carbon atoms in metal matrix is accelerated and the formation of the carbide phases on surface of the parent metal particles begins. The third stage of synthesis completes the formation of carbide. As revealed, the processing time required for the complete transformation of the initial components to the carbide correlates with the enthalpy of its formation, and the fields of mechanical stress are relaxed over two main channels: heating and grinding. As found out, the carbides of *d*-transition metals studied in this work are formed mainly due to self-supporting

reaction at milling. The efficiency of using carbon nanotubes in the fabrication of nanocomposite materials with improved functional characteristics is shown. As revealed, the reaction milling is effective for the synthesis of multicomponent carbides (substitutional solid solutions).

Keywords: mechanochemical processing, carbon nanotube, carbide, solid solution, x-ray diffraction, electron microscopy.

1. Introduction: Mechanochemical Processing

1.1. Brief Historical Perspective

Use of mechanical energy to grind down various materials dates back to the beginning of human history. Research activity in the field of mechanochemical processing (MCP) has a long history with the first publication dating back to 1892 when an American chemist M. Carrey Lea has shown that the halides of gold, silver, platinum and mercury decomposed to halogen and the metal during fine grinding in a mortar [1]. This study clearly established that chemical changes could be brought about not only by heating but also by mechanical action. No less reason to consider M. Faraday, who studied the acceleration of dehydration of the crystalline hydrates during mechanical action, the founder of mechanochemistry. But the use of mechanically activated processes, however, dates back to the early history of mankind, when fires were initiated by rubbing flints against one another. W. Ostwald coined the term 'mechanochemistry' in 1891 in the 'Textbook of General Chemistry', which, in particular, considered various types of stimulation of chemical processes. While the scientific basis underlying MCP was investigated from the very beginning, applications of MCP products were slow to come about, mostly because of limitations on the productivity of MCP reactors, purity of the products and the economics of the process.

It is now accepted that the MCP technique embraces three different processes, mechanical alloying, mechanical milling, and reaction milling. All these three processes involve cold welding, fracturing and rewelding of powder particles during repeated collisions with grinding balls in a high energy milling device. However, depending on the actual process, other features may be present.

So far, an interest in research in the field of mechanochemistry is high since the mechanochemical processing is a rather simple and effective technique for obtaining a wide class of compounds and novel nanocomposite materials (NCM). For the moment, scientists concentrate their efforts not only on the technological features and fundamental principles of MCP process, but also on the establishment of application fields of materials obtained as a result of this synthesis method.

1.2. Features of the Mechanical Processes at MCP

The processes taking place at MCP are initiated by the mechanical action of the reactor equipment (ball mill) on the test substance. They belong to the non-equilibrium phase transformations and occur at room temperatures, in which the redistribution of atomic components by *the normal diffusion mechanism* is absent. However, since the mechanical action usually causes intense cold plastic deformation of a substance, then an additional point or linear defects appear in this substance. The presence of these defects creates conditions for the transport of atoms on a distance much larger than interatomic due to the process of *strain-induced mass transfer*.

It is known that the temperature is one of the parameters determining the mobility of atoms in metals and alloys under normal conditions. Increase of the temperature leads to an increase in the diffusion mobility of atoms. Such factors as radiation, which leads to an increase of the number of point defects [4, 5], phase (martensitic) transformations [6–9], and plastic deformation of substance [10–13] resulting in a growth of the diffusion mobility of atoms by several orders [14] are necessary to note among other ways to increase the rate of diffusion processes.

The transfer of large amount of energy accompanies an intense deformation action on a substance in a ball mill, resulting in the formation of special locally heterogeneous states that are caused by saturation of the substance by defects and high tensions on sub-micron and nanoscaled structure elements. Formation of such local stressed states in a substance results in the two processes, namely: *the diffusionless collective displacement of atoms*, and the process of *anomalous low-temperature diffusion* of disordered displacement of atoms at a distance much larger than interatomic [11–13, 15–17].

Since mechanical treatment of a substance in a ball mill at MCP is purely pulsed process, the mechanical processes described above, as well as the chemical processes described below, do not occur at the whole time; but only at the moment of impact and during the period of relaxation of the stress field, that takes place on different channels depending on the synthesis conditions [18].

1.3. Features of the Chemical Processes at MCP

The mechanical processing in ball mills is the most common and quite simple procedure in mechanochemistry. That is why both the mechanics and the physics of the processes occurring at grinding are the subject of various studies, most of which are devoted to optimizing the milling stage in order to obtain the maximum reaction surface of a substance with the minimal energy consumption.

Two principles already mentioned are the basis of the research of processes occurring at mechanochemical processing, namely: the impulse nature of process (the emergence of stress field and its relaxation [19–22]) and the local character of the mechanical action on the substance (at processing, the stress field does not occur in the entire volume of a substance, but only in the zone of particles contact [23–25]). The aim of such studies is to determine the boundaries of a region where the stress field is formed at mechanical action, existence time and a mode of this region (for example, jump in pressure [26, 27]), as well as the determination of relaxation channels of the stress field. In general, relaxation of the stress field can lead to an increase in the local temperature, to the formation of new metastable phases, to polymorphic transformations in the substance, to the formation of structural defects, to the emergence of a new active surface, etc. [28].

If the substance that is mechanochemically treated is one-component or single-phased the relaxation of a stress field can be accompanied by the heat release, the formation of metastable and polymorphic phases, the formation of a new developed particle surface, the appearance of defects in the substance, and also by its amorphization.

Part of each of these relaxation channels depends on the conditions and magnitude of the mechanical load (load rate and an amount of energy applied), the physical properties of a substance treated, processing temperature, etc. Sometimes the relaxation channel may change in the process. For example, an increase in the growth rate of the main cracks of oxysalts crystals at MCP is accompanied by a change in the mechanism at the tip of crack, i.e., thermal decomposition is replaced by mechanochemical one [29, 30]. Change in the size of the particles that are mechanically processed is accompanied by the transition from their crushing to the process of plastic deformation [31, 32]. The grinding of a substance at MCP leads to obtaining a maximum reaction surface powder at minimum energy costs that reduces the activation energy of the subsequent chemical transformation along with the accumulation of energy in the form of defects.

Generally, there are two types of mechanical activation process. It is referred to a process of the first type if a cumulative time of mechanical action, formation of stress field and its relaxation is longer than a time of chemical reaction (*mechanochemical process*). On the contrary, in the course of a process of the second type, the time of mechanical action and the formation of stress field is shorter than the time of chemical reaction, or in general, these processes are separated in time (the process of mechanical activation or *reaction milling*).

At reaction milling due to plastic deformation of a substance processed the accumulated energy is usually consumed to the formation of defects in activated crystals: dislocations, atomic and ionic vacancies.
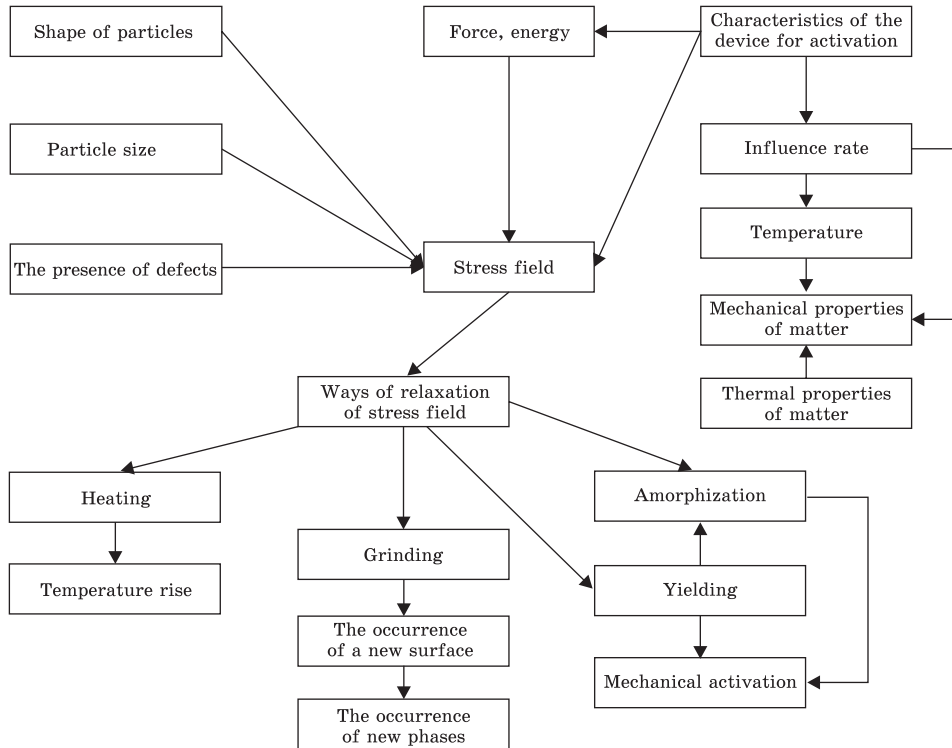
Fig. 1. Schematic representation of the stress fields formation factors arising at reaction milling the main channels of their relaxation

In addition, a significant deformation of the crystal lattice of initial material can lead to the destruction of interatomic bonds, which results in the formation of free radicals in covalent crystals, and to amorphization of molecular crystals.

If a multicomponent powder blend is mechanically treated then the supersaturated solid solutions and stable or metastable inorganic compounds [33–36] may form as a result of solid state mechanochemical reactions between initial components (*mechanical alloying*). In addition, the main factors that determine the possibility of solid solutions formation by mechanical alloying are the similarity of the atom sizes of components and correspondence of their crystalline structures.

It was shown that MCP proceeds by a diffusion mechanism, but unlike the normal diffusion process, it carries with abnormally high values of diffusion coefficient of the atomic components. This type of diffusion has been termed 'deformation atomic entanglement' or 'ballistic diffusion'. Its mechanism is significantly different from the mechanism of normal diffusion, which is determined by the gradients of component concentrations. There is still no single thought about the mechanism of

deformation atomic entanglement. It is assumed either that the diffusion at mechanochemical synthesis is carried out on the interstitial positions in the lattice [37] or that the channels of this diffusion are dislocations, the amount of which in the case of MCP is constantly increasing [38].

Effect of the above factors on formation of the stress field, as well as the main ways of their relaxation, are schematically depicted in Fig. 1. In this case, the left side of scheme visualizes the processes of grinding, and the right part characterizes the reaction milling.

Thus, the look back review of processes that are implemented in mechanochemical processing and the mechanisms governing these processes, revealed the promising use of mechanochemical method for low temperature synthesis of high-temperature carbide phases. In this paper, we present experimental data on the MCP synthesis of two-component transition metal carbides in a high-energy planetary ball mill using the carbon nanotubes as a carbon component of the charge.

2. Materials and Methods

2.1. Source Materials

Charge of the required composition of the initial metals and multiwall carbon nanotubes (CNT) was used in the mechanochemical synthesis of carbides and composite materials studied. *d*-transition metals employed in a synthesis are summarized in Table 1 (purity of metals is no less than 99.95% by weight). Fig. 2 shows as an example the morphology of the iron and copper powders used. Micrographs obtained by scanning electron microscopy (SEM) demonstrate the uniform size distribution of metal particles and an absence of coalescent agglomerates. SEM images of other initial metals are similar to those presented at Fig. 2. Besides, the calibrated metal filings were used as initial metal materials for reaction milling of the *Me*−CNT carbides (*Me* = V, Y, Zr, Hf, Ta), Table 1.

The multiwalled carbon nanotubes used in this study as a carbon component of the charge were synthesized by catalytic chemical vapor deposition method (CVD) at TM Spetzmash Ltd (Kyiv, Ukraine). Al_2O_3, MoO_3 and Fe_2O_3 oxides were used as the catalysts for the CNT production. Propylene obtained by dehydration of isopropyl alcohol was a source of the carbon. Parameters of CNTs are as follows: the average diameter is 10−20 nm, the specific surface area (determined by argon desorption method) is 200−400 m^2/g and their poured bulk density varies from 20 to 40 g/dm^3. TEM image of carbon nanotubes is shown in Fig. 3. It is possible to observe the presence of CNT agglomerates, which essentially complicates the process of manufacturing composites with a uniform CNT distribution by traditional methods of powder metallurgy.

2.2. Mechanochemical Processing

Elemental metal powders (or metal filings) and multiwall CNTs were mixed to give the desired average composition and sealed in a vial (height of 70 mm, diameter of 50 mm) under an argon atmosphere. The high energy planetary ball mill used for MCP is a custom made model developed at the Metal Physics and Ceramics Laboratory of the Taras Shevchenko National University of Kyiv. Hardened stainless steel balls (11 units of 15 mm diameter) with a ball-to-powder weight ratio of 40 : 1 were used. The vial temperature was held below 375 K during the experiments by air cooling. The milling process was cyclic with 15 min of treatment and 30 min of cooling time. The rotation speed was equal to 1480 rpm; the acceleration was about 50 g; the pressure for a substance particle reached 5 GPa.

2.3. X-Ray Diffraction Methods

The full complex of the x-ray diffraction methods (XRD) has been used to study the kinetics of phase transformations of the initial charge at mechanochemical processing in a ball mill as well as structural changes in phase components (lattice periods, presence of vacancies, etc.), and the parameters of real structure (crystallite size, deformation of the crystalline lattice) of the synthesized carbides.

The XRD data were collected with DRON-3 or DRON-4 automatic diffractometers (CuK_α or CoK_α radiation, respectively) for the proof samples selected after a certain milling time. The diffraction patterns have obtained in a discrete mode under the following scanning parameters: observation range $2\theta = 20-130°$, step scan of $0.05°$, and counting time per step at 3 s.

The original software package developed by us for the automated DRON equipment has been used for analysis and interpretation of the
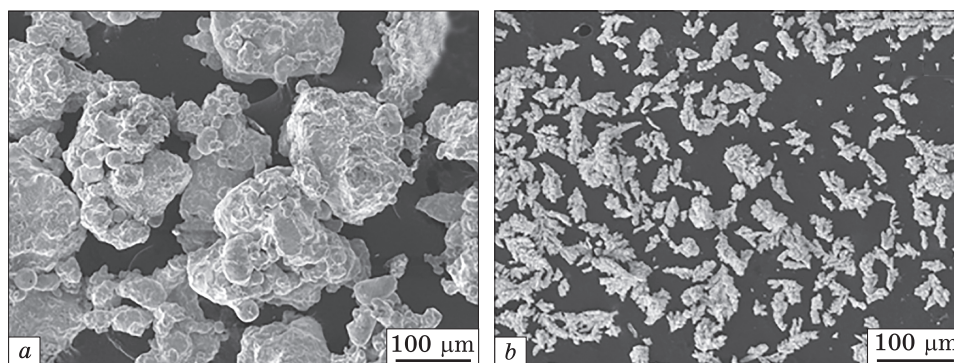

Fig. 2. SEM micrographs of the source powders: *a* — iron ($\approx$200 μm of size) and *b* — copper ($\approx$60 μm of size)
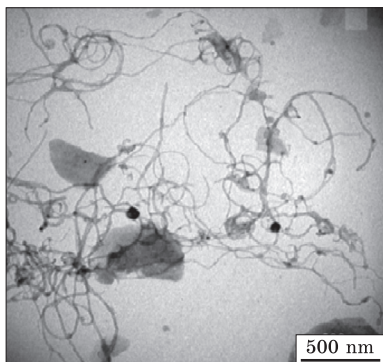
Fig. *3*. TEM micrographs of the multiwalled carbon nanotubes

x-ray diffraction data obtained. This package contains a full range of standard Ritveld analysis and is intended for solving different XRD tasks, namely, determination of both peak positions and integral intensities of the Bragg reflections by means of full profile analysis; carrying out qualitative and quantitative phase analysis using PDF data for phase identification and the least square method for lattice constants refinement; testing of the structure models and refining crystal structure parameters (including coordinates, atomic position filling, texture, etc.). The mathematical algorithms realized for these calculations are

Table 1. **Crystallographic data of phases formed in *Me*−CNT charge after 60 min of processing in a ball mill**

| *Me* | | Initial material | Structure type | Lattice parameter, nm | | | | R_B | CNT content calculated, at.% |
				Product synthesized		Initial metal			
				a	*c*	*a*	*c*		
3*d*	Ti	Powder, 90−125 μm	Mg	0.2954(2)	0.4685(3)	0.2951(2)	0.4686(2)	0.112	?
	V	Filings, <200 μm	α-Fe	0.3027(3)		0.3030(3)		0.029	16(2)
	Fe	Powder, <200 μm	α-Fe	0.2866(2)		0.28665(4)		0.0029	9(2)
	Co	Powder, <80 μm	Mg	0.2508(2)	0.4076(8)	0.2507(2)	0.40695(4)	0.110	?
	Ni	Powder, <80 μm	Cu	0.35225(2)		0.3524(1)		0.012	5(1)
	Cu	Powder, <60 μm	Cu	0.3638(2)		0.36149(3)		0.024	2(1)
4*d*	Y	In pieces	Mg	0.3641(2)	0.5747(5)	0.36474(3)	0.57306(4)	0.092	?
	Zr	Filings, <200 μm	Mg	0.3239(2)	0.5148(2)	0.3232(1)	0.5147(1)	0.098	?
	Nb	Powder, <40 μm	α-Fe	0.33043(2)		0.3300(1)		0.013	10(2)
	Mo	Powder, <40 μm	α-Fe	0.3147(3)		0.3147(1)			5(1)
5*d*	Hf	In pieces	Mg	0.3190(4)	0.5044(5)	0.3196(2)	0.5051(1)	0.086	?
	Ta	Filings, <200 μm	α-Fe	0.3310(2)		0.33013(3)		0.025	4(1)
	W	Powder, <40 μm	α-Fe	0.3168(3)		0.31652(3)			3(1)
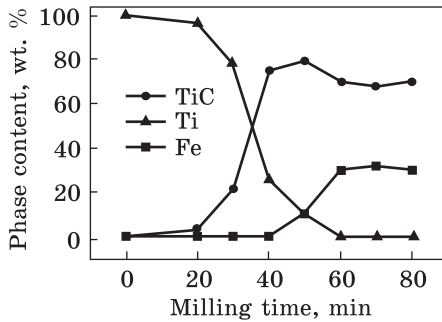
Fig. 4. Phase composition (wt.%) of the Ti−CNT charge reaction milling vs. the processing time
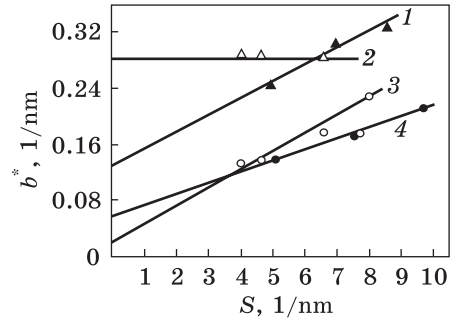
Fig. 5. The Williamson−Hall plots for phases of the Fe−TiC samples: (*1*) α-Fe (120 min of processing), (*2*) TiC (120 min of processing), (*3*) TiC (compacted sample), (*4*) α-Fe (compacted sample)

similar to those used in WinCSD software [39]. More information about this package is available in Ref. [40].

Typical kinetic curve of the TiC phase transformations at MPC is shown in Fig. 4. It should be noted that test samples selected after 60 minutes the processing contain Ti and TiC phases along with a certain amount of iron (Fig. 4) that appears in the sample due to the wear debris.

Similar curves that visualize the course of the synthesis process were obtained for each carbide phase synthesized.

Crystallites size and deformation of the crystal lattice of the phases synthesized were determined through the Williamson−Hall method [41]. The average values of the grain size D and deformation of the crystal lattice ε of the carbides synthesized were estimated via the peak broadening. The Williamson−Hall graphs are plotted as dependencies of scaled broadening of Bragg's reflections, $b^*(2\theta) = \beta(2\theta)(\cos\theta)/\lambda$, on scattering vector $S = (2\sin\theta)/\lambda$ for each test sample have been studied, where θ is the Bragg's reflection, λ is the wavelength, $\beta(2\theta) = (FWHM_{\exp}^2 - FWHM_R^2)^{1/2}$ is an intrinsic broadening (where $FWHM_{\exp}$ and $FWHM_R$ are experimental and instrumental broadening, respectively).

Typical Williamson−Hall graphs plotted for the phases present in the Fe-TiC composite (see section 4.1.1) are presented in Fig. 5. The average grain size D could be found by extrapolating the $b^*(2\theta)$ dependencies onto $S = 0$ axes as $D = 1/b^*(2\theta)$ at θ = 0. The average microdeformation of crystal lattice ε could be found from slope of the $b^*(2\theta)$ straight line versus S as $\varepsilon = b^*(2\theta)/2S$.

Taking into account the fact that ε(*S*) dependence obtained for the TiC phase is a horizontal line (Fig. 5) one can conclude that only a fine structure of this carbide (and not a deformation of its crystalline lattice) makes an influence on the diffraction peaks broadening of this phase.

2.4. Electron Microscopy

The method of scanning electron microscopy (SEM) was used both to analyze the microstructure of the synthesis products and to determine the elemental composition of the phase components. SEM exanimation of the samples was carried out using JEOL JAMP-9500F field emission auger microprobe operated at 10 kV or a scanning electron microscope ZEISS EVO 50XVP operated at 15 kV, which offers the flexibility of optional analysis functions such as an energy-dispersive x-ray spectroscopy (EDS).

The detailed analysis of samples microstructure was carried out by transmission electron microscopy (TEM). TEM images of the CNTs and composites after milling were obtained with a transmission electron microscope SELMI PEM-125K operated at 100 kV.

3. Characteristic of Interaction in the Metal–CNT Binary Systems

Materials with carbon content are widely used in industry mainly as the iron based alloyed solid solutions (steels). Carbides of transition metals keen demand as wear-resistant coatings and fillers of metal matrices when creating solid wear-resistant materials (solid alloys, etc.). Traditionally, the graphite or carbon black are used as a carbon component for the manufacture of these materials. However, the carbon nanotubes (CNTs), which are characterized by unique combination of the mechanical characteristics due to their size, geometry and crystal structure [42–44] look as a promising component of novel functional materials with improved mechanical, thermal, and magnetic properties. Carbon nanotubes form agglomerates in the initial state, which usually do not undergo destruction and grinding that essentially complicates their use in the development of materials. However, mechanochemical processing of the CNT-containing charge in a high-energy ball mill allows us to produce a variety of commercially useful and scientifically interesting materials since CNTs are amorphized under processing and homogeneously distributed in volume. Due to the substantial grinding of the charge and the destruction of carbon nanotubes, such processing ensures high reactivity of the components. The interaction of the metal with CNTs that occurs at the same time leads to the formation of supersaturated interstitial solid solutions and/or carbide phases, usually with a modified structure and improved properties.

The authors of this review have achieved a certain success in synthesis of the carbide phases by mechanochemical processing of the *Me*–CNT charge in a high-energy ball mill [45–47] and these results are discussed herein.

3.1. Solubility of the Carbon Nanotubes in d-Metals

Studying kinetics of the transition metal carbidization, a special attention was paid to identify the changes in the initial metals occurring in their interaction with carbon nanotubes during mechanohemical process. For this purpose the test samples selected after 60–90 min of processing of the initial charge in a ball mill have thoroughly tested under XRD method.

According to the XRD data, at the initial stages of mechanochemical processing the diffraction patterns from the milling products are similar to those form the initial metals. Indeed, Figs. 6, 7 present diffraction patterns for three test samples, representing three different type structures for the metals studied, namely, the Fe–CNT (α-Fe-type structure), Cu–CNT (Cu) and Zr–CNT (Mg). It should be noted that according to the XRD results the calculated lattice parameters for main phases existing in the *Me*–CNT blends practically correspond to those for initial metals (Table 1) after 60 min of processing.

The crystal structure calculations for the milling products selected after 60 min of processing have revealed that the best agreement between experimental and calculated intensities of reflections (R_B factors are less than 0.03, Table 1) can be achieved for a trial model in which atoms of carbon are implanting in octahedral pores of Cu and α-Fe-type structures with simultaneous appearance of vacancies in the metal atom positions. More specifically, the following model is proposed for f.c.c.-metals: the *Fm3m* space group, *Me* atoms are placed in $4(a)$ (0 0 0); C atoms are placed in $4(b)$ (0.5 0.5 0.5) (the occupation of $4(a)$ position is slightly less than 1, and $4(b)$ position is only partially filled with carbon atoms). A model proposed for b.c.c.-metals is as follows: the *Im3m* space group, *Me* atoms are placed in $2(a)$ (0 0 0); C atoms are placed in $6(b)$
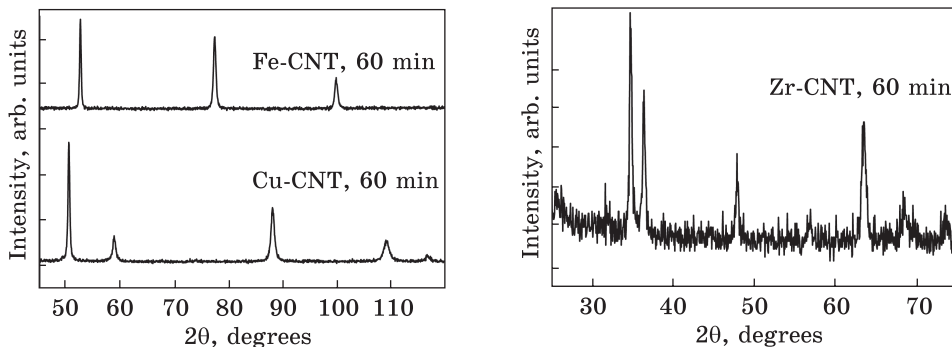

Fig. 6. XRD patterns of the Fe–CNT and Cu–CNT powders treated for 60 min in a ball mill, CoK_α radiation

Fig. 7. XRD pattern of the Zr–CNT charge after 60 min of the processing, CuK_α radiation

CuC$_x$ structure

C.N. 6, octahedron

C	Cu	0.1819
	Cu	0.1819
	Cu	0.1819
	Cu	0.1819
	Cu	0.1819
	Cu	0.1819

C.N. 6, octahedron

C	C	1.433
	C	1.433
	C	1.433
	C	1.433
	Fe	1.433
	Fe	1.433

α-Fe$_3$C$_x$ structure

Zr$_3$C$_x$ structure

C.N. 6, octahedron

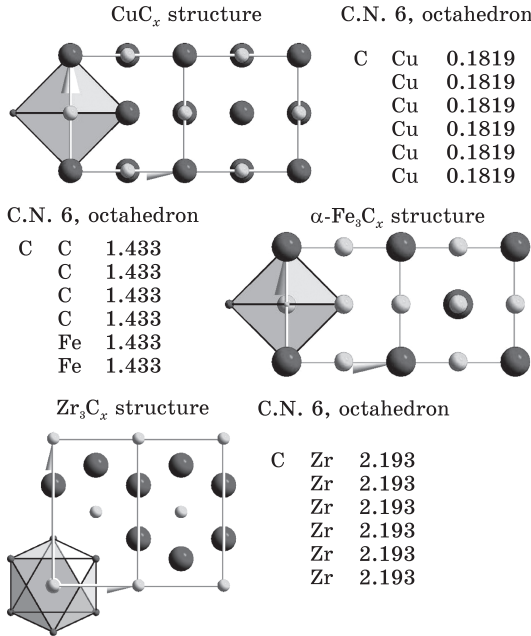| C	Zr	2.193
	Zr	2.193
	Zr	2.193
	Zr	2.193
	Zr	2.193
	Zr	2.193

Fig. 8. Structure mappings of interstitial solid solutions on the *XY* axis (see also this figure at the web-site of the journal)

(0.5 0 0). Similarly to f.c.c.-structures, the occupation of 2(*a*) position is slightly less than 1, and position 6(*b*) is only partially filled with carbon atoms. Thus, the cubic phases studied are *Me*C$_x$ interstitial solid solutions with implanting the carbon atoms into lattices of the initial metal. Mappings of two typical structures of cubic CuC$_x$ and FeC$_x$ interstitial solid solutions of are shown in Fig. 8. The calculated amounts of carbon, which is implanting in the octahedral pores of structures, are listed in Table 1. In the case of phases with hexagonal crystal structures, calculations made in the Mg-type structure did not lead to a correct result even taking into account the existing of texture (*R$_B$* factor was higher than 0.09, Table 1). Therefore, it was suggested that the internal rhombic deformation of the Mg type structure is inherent to these phases. Thus, further calculations were carried out within the framework of an orthorhombic lattice with $a_{romb} = a_{hex}$, $b_{romb} = a_{hex}\sqrt{3}$, $c_{romb} = c_{hex}$, *Cmcm* space group *Me* atoms are placed in 4(*c*) (0 *z* 0.25); C atoms are placed in 4(*a*) (0 0 0). Similarly to the above cubic structures, occupation of 4(*c*) position is slightly less than 1 while 4(*a*) position is only partially filled with carbon atoms. Calculated values of the crystallographic

Table 2. **Crystallographic parameters of interstitial solid solutions on the base of hexagonal metals**

Me	Lattice parameter, nm					*z*	*R$_B$*	CNT content calculated, at.%
	Mg type structure		ZrC$_x$ type structure					
	a	*c*	*a*	*b*	*c*			
Ti	0.2954 (2)	0.4685 (3)	0.2945 (3)	0.5111 (5)	0.4687 (3)	0.303 (2)	0.051	8 (2)
Co	0.2508 (2)	0.4076 (8)	0.2498 (2)	0.4342 (3)	0.4063 (4)	0.333 (3)	0.056	4 (1)
Y	0.3641 (2)	0.5747 (5)	0.3633 (2)	0.6320 (5)	0.5741 (5)	0.318 (5)	0.058	12 (1)
Zr	0.3239 (2)	0.5148 (2)	0.3242 (4)	0.5590 (6)	0.5139 (5)	0.318 (4)	0.055	7 (2)
Hf	0.3190 (4)	0.5044 (5)	0.3209 (5)	0.5538 (6)	0.5051 (5)	0.314 (5)	0.051	1

characteristics of the distorted hexagonal phases taking into account the texture are contained in Table 2. It should be noted that this structural model, describing the above interstitial solid solutions, could be considered as a new ZrC_x type structure.

Therefore, performed calculations have shown that the orthorhombic model better describes the crystal structures of the interstitial solid solutions formed on the base of initial metals with Mg-type structure. The projection of this structure on the XY plane is shown at Fig. 8. It is seen that the carbon atoms have an octahedral environment of metal atoms.

Thus, XRD study showed that the formation of the interstitial solid solutions with carbon atoms implanted in the octahedral pores of the crystal structures of the initial metal takes place at the first stage of the Me−CNT charge processing in a ball mill. In this case, the metal sub-lattices of all solid solutions become vacant. Moreover, the lattices of the metals with Mg-type structure become essentially internally deformed.

It is natural to assume that the main factor regulating the formation of these interstitial solid solutions is the diffusion of the carbon atoms into a metal lattice. Indeed, the analysis provided has shown that the amount of CNTs, which are implanting in the crystal lattice after 60 min of milling (Table 3), correlates well with the values of the activation energy of carbon diffusion in the corresponding metals independently on the crystal structure of the metal matrix, (Fig. 9).

Table 3. **Solubility of the carbon in solid solutions obtained by MCP and solubility of the carbon in metals at high temperatures**

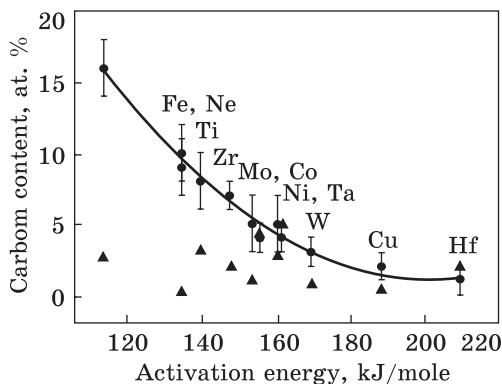| *Me*		Carbon Solubility, at.%		Activation energy of diffusion, $kJ \cdot mole^{-1}$
		Calculated carbon content in materials studied	Maximum carbon solubility in the equilibrium diagram	
3*d*	Ti	8(2)	3.1	139
	V	16(2)	2.6	113
	Fe	9(2)	0.02	134
	Co	4(1)	4.3	155
	Ni	5(1)	2.7	160
	Cu	2(1)	0.03	188
4*d*	Y	12(1)	8.8	?
	Zr	7(2)	2.0	147
	Nb	10(2)	0.26	134
	Mo	5(1)	1.1	153
5*d*	Hf	1	2.0	209
	Ta	4(1)	0.1−7.5	161
	W	3(1)	0.7	169

Fig. 9. The dependence of carbon content in *d*-metal based solid solutions on the activation energy of the C diffusion in a metal. Solid solutions obtained by mechanochemical synthesis are marked by circles. The maximum solubility of carbon (from to the data for corresponding state diagrams) is marked by triangles

According to the data obtained it is clear that if in the state of thermodynamic equilibrium, the solubility of carbon in the initial *d*-metals at high temperatures (above 1500 °C) usually does not exceed 3−4 at.%, than the processing of the *Me*−CNT charge in a ball mill leads to the formation of the carbon-rich metastable solid solutions. The solubility of carbon in these supersaturated solid solutions is usually substantially higher than its solubility in a stable state (Fig. 9). During formation of supersaturated solid solutions, the amorphous carbon is implanting in the octahedral pores of structures of known α-Fe and Cu types, as well as in the octahedral pores of a rhombic distorted Mg type structures.

3.1.1. Carbides of IIIb, IVb and Vb Groups

Process of formation of IIIb, IVb and Vb monocarbides with the NaCl-type structure as well as carbides existing in the Y−CNT system have studied. Type and characteristics of the initial metals used are summarized in Table 1.

Synthesis of the TiC, ZrC, HfC, VC, NbC, and TaC Monocarbides. A set of experiments on the mechanical alloying of the equiatomic *Me*:CNT (1:1) mixtures was carried out in order to study the *Me*C process of formation (Table 1). According to the XRD results *Me*C phase is the only constituent of the test samples selected after 210−400 min of processing in a planetary ball mill (samples do not contain any traces of initial metals). The refined lattice parameters for monocarbides synthesized are given in Table 4. It should be noted that the *Me*C lattice parameters obtained here are significantly lower than those which are inherent to conventional monocarbides (Table 4). Fragments of the typical XRD patterns obtained for the final milling products are shown in Fig. 10. Average values of the crystalline size D and lattice deformation ε were defined (Table 5) from the broadening of the *Me*C peaks on XRD

patterns. The calculations have revealed that D values for mechanically alloyed MeC are equal to 10–30 nm.

It should be noted that according to the phase analysis results the formation of MeC monocarbides is accompanied by wear debris of steel vial and balls. Therefore, some test samples along with the MeC phase contain an admixture of the α-Fe phase (marked as 'x' at Fig. 1), the amount of which increases with processing time increasing. In order to eliminate the samples from the iron contamination, we treated all milled powders in a 50% solution of hydrochloric acid and 5 times washed in

Table 4. **Crystallographic data of *Me*C monocarbides synthesized by the reaction milling of *Me*–CNT charge**

Carbide	Experimental data for Me–CNT charge				
	Reaction milling	Annealing at 700 °C after reaction milling			
	Lattice parameters, a, nm	Lattice parameters, a, nm	R_B	Me content, at.%	Formula
TiC	0.4297(9)	0.4301(1)	0.037	48.3 XRD 48.8 EDS	Ti$_{0.97}$C
ZrC	0.4651(8)	0.4655(1)	0.037	49.6 XRD 49.2 EDS	Zr$_{0.99}$C
HfC	0.4589(1)	0.4588(1)	0.013	50.0 XRD	HfC
VC	0.4154(5)	0.4156(1)	0.034	47.0 XRD 46.6 EDS	V$_{0.94}$C
NbC	0.4447(2)	0.4446(1)	0.022	46.8 XRD 45.3 EDS	Nb$_{0.92}$C
TaC	0.4435(9)	0.4436(2)	0.035	46.7 XRD 47.7 EDS	Ta$_{0.94}$C

| Carbide	Reference data for carbides obtained from Me-graphite charge				
	Reaction milling		Conventional carbides		
	Lattice parameters, a, nm	Formula	Lattice parameters, a, nm	Me content, at.%	Formula
TiC	0.4311 0.4323	TiC TiC$_{0.88}$	0.4327	51.3	TiC$_{0.95}$
ZrC	0.4651 0.4695	ZrC$_x$ ZrC$_{0.83}$	0.4693	51.3	ZrC$_{0.95}$
HfC	0.4626	HfC$_x$	0.4642	50.0	HfC
VC	0.4133 0.4416	VC$_x$ VC	0.4167	53.1	VC$_{0.88}$
NbC	0.4422 0.4468	NbC$_x$ NbC$_{0.91}$	0.4470	51.3	NbC$_{0.95}$
TaC	–	–	0.4456	50.0	TaC$_{0.95}$
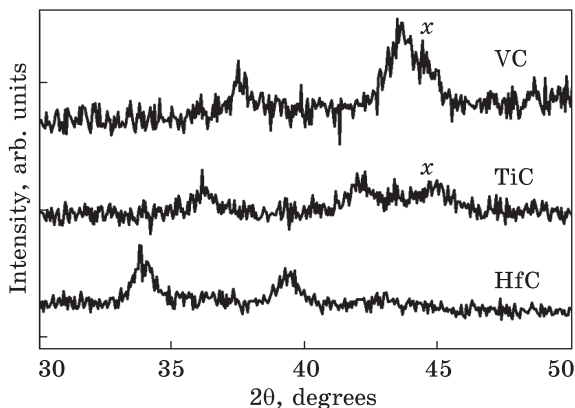
Fig. 10. XRD patterns of the milled *Me*−CNT charge, CuK_α radiation

distilled water away from the FeCl$_2$ precipitate. The purified powders were dried at room temperature for 48 hours. According to EDS data the content of iron in such powders treated in HCl does not exceed 0.2 wt.%.

Unfortunately, due to an essential broadening and small number of diffraction peaks on the diffraction patterns of the final milling products (Fig. 10), it is impossible to refine the crystal structure of the carbides formed correctly. Consequently, the chemically treated samples have been annealed for 2 h at 700 °C under argon atmosphere in order to diminish or even remove additional microdeformations of the crystal lattice, and thus, to improve the overall appearance of the x-ray patterns (Fig. 11). XRD study has revealed that the lattice parameters of the *Me*C monocarbides existing in the annealed samples are similar to those in the final milling products (Table 4), while diffraction peaks on their patterns are significantly sharpened (Fig. 11). The D and ε values for the *Me*C phases after annealing were determined by the Williamson–Hall plot and approximation method. It should be noted that annealing is accompanied by a reduction of the lattice strains, while the crystalline sizes do not change (Table 5).

Table 5. **Crystallite size and deformation of the crystal lattice of the *Me*C carbides formed by the reaction milling of the *Me*−CNT charge**

Carbide	Material synthesized		After annealing at 700 °C	
	Crystallite size, D, nm	Lattice deformation, ε, %	Crystallite size, D, nm	Lattice deformation, ε, %
TiC	24(1)	2.54(5)	22(2)[*]/11(1)[**]	1.15(4)
ZrC	33(3)	1.24(4)	26(2)/13(1)	1.26(4)
HfC	32(3)	2.27(5)	29(3)/4(1)	1.59(5)
VC	10(2)	2.34(5)	12(2)/7(1)	1.45(4)
NbC	13(1)	1.39(4)	8(1)/8(1)	0.47(1)
TaC	19(2)	1.85(4)	14(1)/9(1)	1.73(2)

[*] Calculated by the Williamson−Hall method. [**] Obtained by the approximation method.
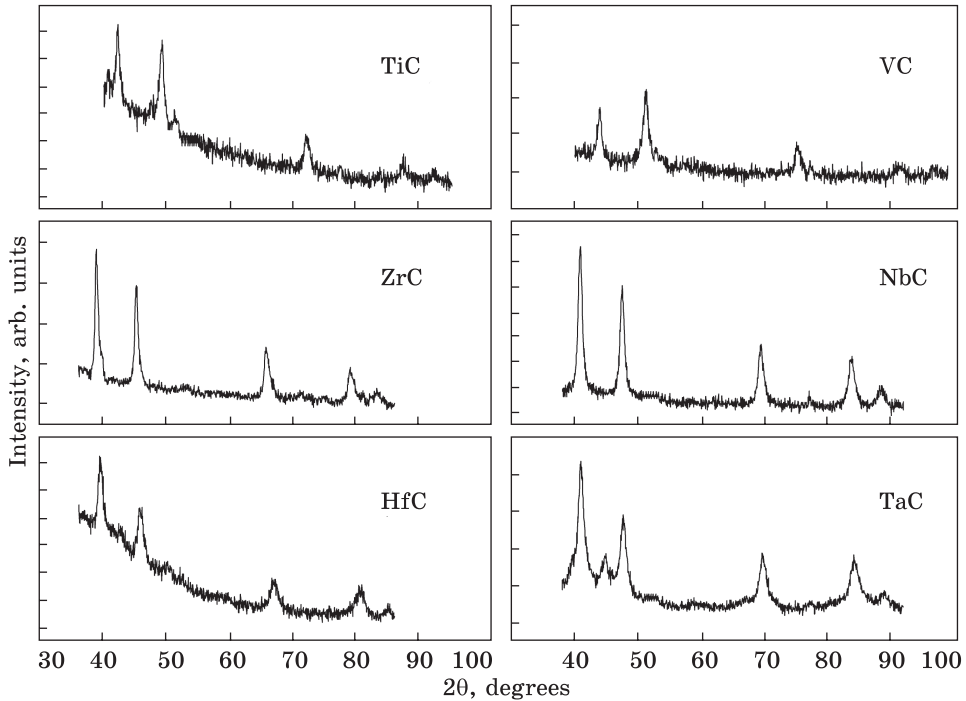
Fig. 11. XRD patterns of the milled *Me*–CNT charge after treatment by HCl and annealing at 700 °C, CoK_α radiation
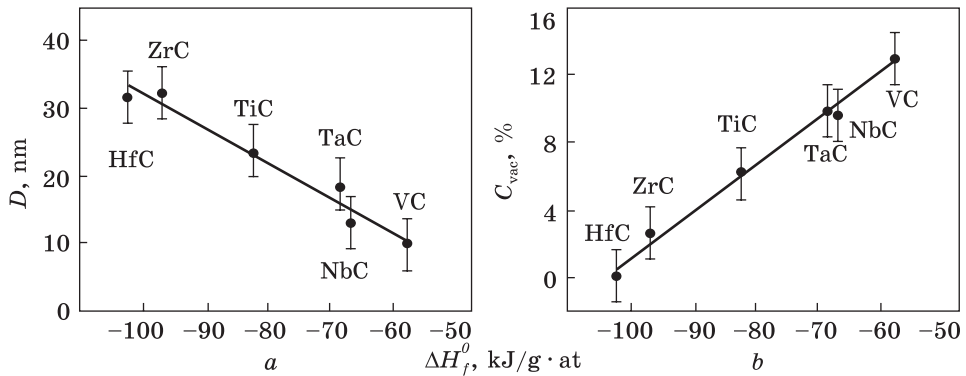

Fig. 12. The dependences of crystallite size D (*a*) and concentration of vacancies C_{vac} (*b*) in a metal sublattice on the enthalpy of monocarbide formation

The XRD results obtained have reviled that the milling time required for a complete transformation of the raw components into a corresponding monocarbide correlates with the enthalpy of its formation ΔH_f^0 (see more details later). Moreover, the enthalpy of monocarbide formation proved to be a suitable parameter to analyse the character of a crystalline size change in these phases. Obviously, the higher the enthalpy of
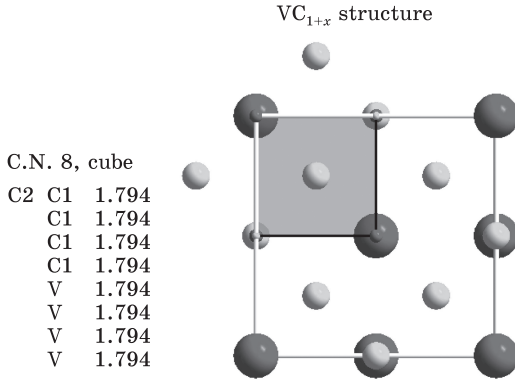
VC$_{1+x}$ structure

C.N. 8, cube

C2	C1	1.794
	C1	1.794
	C1	1.794
	C1	1.794
	V	1.794
	V	1.794
	V	1.794
	V	1.794

Fig. 13. Structure mapping of VC$_{1+x}$ carbide on the *XY* axis (online version of the figure is also available)

formation, the smaller grain size of the corresponding *Me*C phase (Fig. 12, *a*).

Thus, due to the sharpening of diffraction peaks it becomes possible to make a refinement of the crystal structure of *Me*C phases. Calculations required have made in a framework of the NaCl-type structure (*Fm3m* space group): *Me* atoms are placed in 4(*a*) (0 0 0) and C atoms are placed in 4(*b*) (0.5 0.5 0.5). In doing so, we have refined both the occupations of 4(*a*) and 4(*b*) positions by atoms and the isotropic temperature factors. The validity of these calculations was confirmed by the meaning of reliability factor R_B that did not exceed 0.04 for each phase (Table 4). Results of *Me*C crystal structure refinements have revealed the existence of vacancies in 4(*a*) position filled with the metal atoms unlike crystal structure of conventional carbides in which 4(*a*) position is completely filled. In contrast to 4(*a*) position, the 4(*b*) position is only partially filled with carbon atoms in both cases. Presence of vacancies in a metal sublattice results in a significant shift of the *Me*C composition to the carbon side, which was also confirmed by EDS data (Table 4).

However, in addition to the proposed model of NaCl-type structure with 4(*a*) and 4(*b*) positions partially filled by metal and carbon atoms the variant of modified NaCl-type structure, in which the partial filling of 8(*c*) (0.25 0.25 0.25) position by additional carbon atoms is realised,

Table 6. **Distribution of components by the regular point system in *Me*C monocarbides synthesized by MCP**

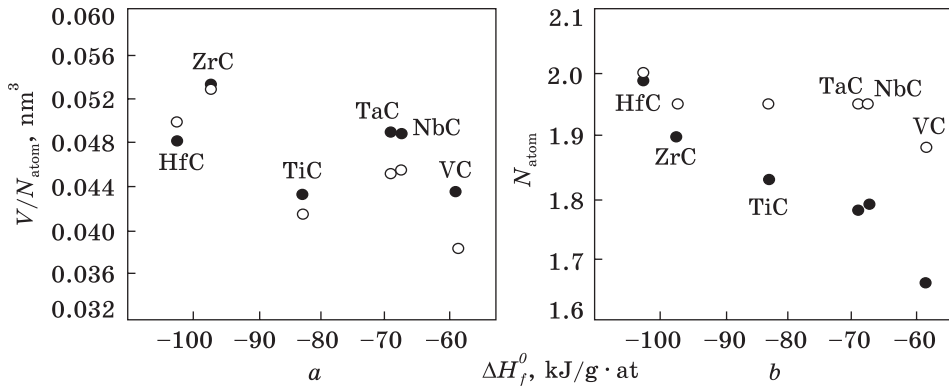| Carbide | Distribution of components | | | R_B |
| | *Me* | Carbon | | |
	4(*a*)	4(*b*)	8(*c*)	
TiC	48.5	48.1	3.4	0.018
ZrC	49.4	48.2	2.4	0.009
HfC	50.0	50.0	0	0.013
VC	46.8	50.4	2.8	0.014
NbC	46.1	52.8	1.3	0.015
TaC	46.7	52.3	1.2	0.021

Fig. 14. The dependences of the calculated value of the total number of atoms in the structures of *Me*C carbides synthesized (*a*) and the partial volume per carbide atom (*b*) on the enthalpy of formation (data for conventional *Me*C are marked as ○, and data for synthesized products are marked as ●)

is possible. The calculations provided have revealed that placing of the additional carbon atoms in $8(c)$ position significantly improves the value of R_B factor, but does not affect the composition of the compound calculated within the common NaCl-type structure. It is worth noting that the carbon atoms placed in $8(c)$ position have a cubic environment consisting of metal atoms and other non-equivalent crystallographically carbon atoms (Fig. 13).

It is possible to calculate the amount of the carbon atoms arranged in cubic pores assuming that the proposed model of the modified NaCl-type correctly describes the structure of *Me*C carbides forming under MCP (Table 6).

Using the data of structural calculations, it is possible to estimate the concentration of vacancies C_{vac} (%) in *Me*C monocarbides as $C_{vac} = C_{Me}/C'_{Me}$, where C_{Me} is the metal content in *Me*C formed under MCP; C'_{Me} is the metal content in a conventional monocarbide. It is shown that C_{vac} values correlates with ΔH_f^0 ones for each *Me*C phase (Fig. 12, *b*). Namely, the more complicated the formation of carbide is, the more vacancies are accumulated in its structure. It is obvious that the presence of vacancies causes a decrease in a total number of atoms N_{atom}, that has calculated as for the *Me*C carbides obtained by MCP, as well as for conventional monocarbides (Table 4). It appeared that the calculated N_{atom} values correlate with the enthalpy of formation for *Me*C carbides (Fig. 14, *a*). Moreover, if this value varies slightly for conventional carbides, then this value increases monotonically for reaction milled carbides (from VC to HfC for which N_{atom} corresponds to the stoichiometric one).

In our opinion, the presence of structural vacancies in the metal sublattice is responsible for a decrease of the lattice parameters of *Me*C
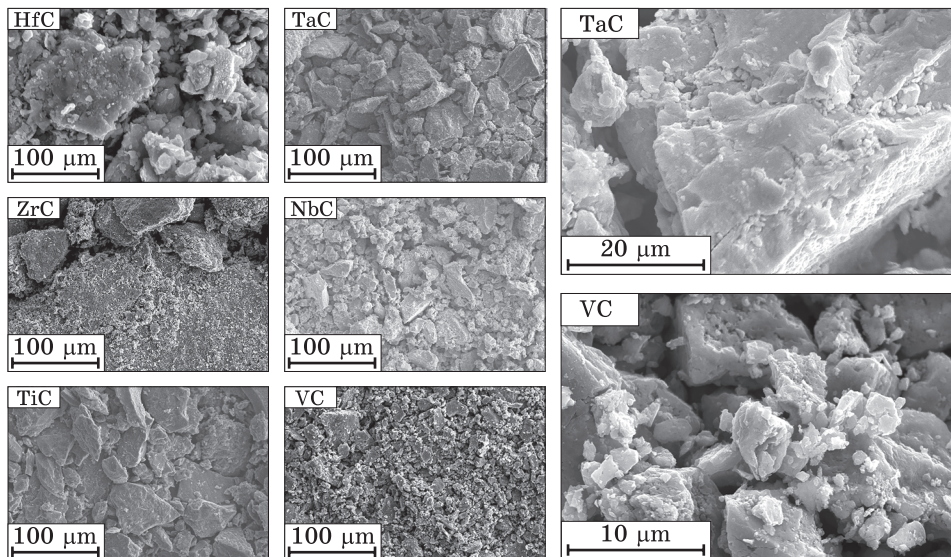
Fig. 15. SEM micrographs of the milled *Me*−CNT charge, where magnifications are ×1000 (*a*) and ×10 000 (*b*)

monocarbides obtained by MCP. Using *a* and N_{atom} values (Table 4) one can calculate the partial volume per one atom in the *Me*C structure as V/N_{atom}. The results of calculations have revealed that the values of partial lattice volume for carbides of the IV*b* group (TiC, ZrC, HfC) synthesized by MCP are very close to those for conventional carbides, while these values for V*b* carbides (VC, NbC, TaC) are somewhat higher (Fig. 14, *b*).

In order to study the morphology of *Me*C particles formed at MCP of *Me*−CNT charge, the chemically purified powders were examined by SEM and EDS methods. As a result, it was shown that all samples do not contain any raw material traces. According to XRD and EDS data, the *Me*C nanocrystals (size of 10−30 nm) form a large powder particles (size of 10−30 μm, Fig. 15), which are the agglomerates of fine crystals. Besides, the smaller size of the *Me*C crystallites (Table 5), the smaller particle is formed (Fig. 15, *a*). Therefore, the largest particles are inherent to HfC, while the smallest ones are observed for VC. Moreover, individual nanocrystalline *Me*C particles could be found on the surface of some big particles that is clearly seen in Fig. 15, *b*, obtained at a higher magnification.

Thus, it was shown that nanoscaled (up to 30 nm) TiC, ZrC, HfC, VC, NbC and TaC monocarbides with the modified NaCl-type structure can be successfully synthesized in a short time (80−400 min) from elemental metals and carbon nanotubes by mechanical alloying (mechano-chemical processing) of the charge in a high-energy planetary ball mill.

Synthesis of the Yttrium Carbides. It is known that the interaction between yttrium and carbon leads to formation of a number of other carbides besides of YC_2 carbide. Data on the composition and crystalline structure of these compounds are quite ambiguous. Particularly, it concerns Y_3C (unknown structure), $YC_{0.44}$ (NaCl-type structure, $a = 0.5115$ nm), Y_2C (Ho_2C, $a = 0.3617$ nm, $c = 1.796$ nm), Y_4C_5 ($PbCl_2$, $a = 0.6574$ nm, $b = 1.1918$ nm, $c = 0.3669$ nm), $Y_{15}C_{19}$ ($Sc_{15}C_{19}$, $a = 0.794$ nm, $c = 1.588$ nm), Y_2C_3 (Pu_2C_3, $a = 0.8233$ nm), YC_2 (CaC_2, $a = 0.3685$ nm, $c = 0.6211$ nm). Exactly this data were used to identify the phases that are formed in the MCP carbides.

According to XRD result, the test sample selected after 60 minutes of processing in a ball mill does not contain any raw charge materials (elemental yttrium) (Fig. 16). The two yttrium carbides, namely, a known cubic $YC_{0.44}$ carbide with $a = 0.5015$ nm and a new YC_x carbide whose diffraction pattern was indexing well in a hexagonal lattice with $a = 0.9041$ nm, $c = 0.6296$ nm make a phase composition of this sample. Further processing of the charge does not lead to a change in the phase composition of MCP products, but lattice parameters of both phases gradually decrease. Thus, for $YC_{0.44}$ carbide: $a = 0.4917$ nm after 120 min of milling and $a = 0.4894$ nm after 180 min. In turn, for YC_x carbide: $a = 0.8978$ nm, $c = 0.6213$ nm after 120 min of treatment and $a = 0.8903$ nm, $c = 0.6171$ nm after 180 min. Particular emphasis needs to be placed on that fact that test sample selected after 180 min of milling contains some amount of α-Fe phase (wear debris). So, one could jump into conclusion that material synthesized has a high strength since the abrasion of the vial and balls clearly certifies it.

Thus, the experiments provided have shown the efficiency of using the carbon nanotubes for mechanochemical processing of the yttrium carbides with enhanced mechanical characteristics.
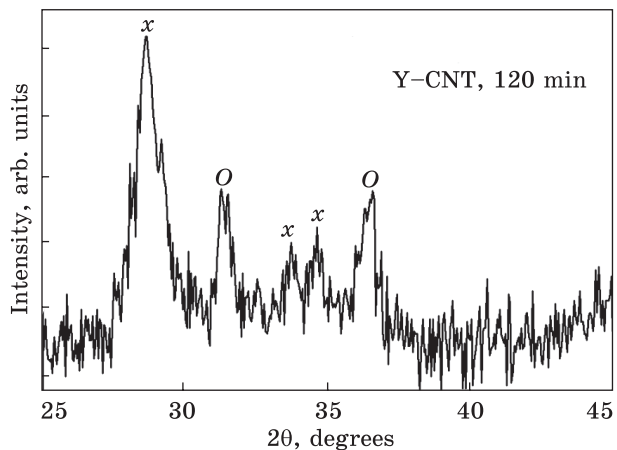

Fig. 16. Fragment of the diffractogram of the Y–CNT charge after processing in a ball mill, CuK_α radiation. The reflections of the YC_x and $YC_{0.44}$ carbides are marked as '*x*' and '*O*', respectively

3.1.2. Carbides of VIb Group

To study the process of WC and Mo_2C carbides formation a set of experiments on mechanical alloying of the mixtures containing initial metal powders and multiwall nanotubes as the carbon component (*Me*:CNT ratio is equal to 1:1 for WC and to 2:1 for Mo_2C) has been performed. Initial metals used in MCP experiments are characterized in Table 1. In order to control the phase transformations occurred during the charge milling, the phase composition of the test samples selected after each 1−2 h of processing have studied. According to the XRD results, all test samples processed up to 4 hours in a ball mill contain no other phases except an initial metal.

Synthesis of the Mo_2C Carbide. According to Ref. [62], three polymorphous modifications are inherent to Mo_2C carbide, namely, high temperature (1440−2522 °C) Mo_2C with W_2C-type structure, high temperature (1200−1440 °C) Mo_2C with own type structure (distorted ζ-Fe_2N-type structure) and low temperature (<1200 °C) Mo_2C.

The diffraction patterns of the test sample processed for 4 hours and 5 hours in a ball mill (Fig. 17) are similar to each other and are

Table 7. **Crystallographic data for W_2C and Mo_2C carbides formed after 4 hours of processing in a ball mill [47]**

Atom	Site	Site occ.	x	y	z
W_2C (ζ-Fe_2N-type structure)					
W	6*k*	0.93(1)	0.333(1)	0	0.280(3)
C (1)	2*d*	1.00(1)	0.333	0.667	0.5
C (2)	1*a*	1.00(1)	0	0	0
Space group			$P31m$ (no. 162)			
Lattice parameter, nm			$a = 0.5168(3); c = 0.4710(4)$			
Independent reflections			27			
Total isotropic B factor, nm^2			$B = 1.80(2) \cdot 10^{-2}$			
Calculated content, at.%			65.1(3) W + 34.9(3) C			
Reliability factor			$R_B = 0.049$			
Mo_2C (ζ-Fe_2N-type structure)					
Mo	6*k*	0.80(2)	0.333(1)	0	0.250(3)
C (1)	2*d*	1.00(1)	0.333	0.667	0.5
C (2)	1*a*	1.00(1)	0	0	0
Space group			$P31m$ (no. 162)			
Lattice parameters, nm			$a = 0.5174(3), c = 0.4744(4)$			
Independent reflections			16			
Total isotropic factor B, nm^2			$B = 1.92(6) \cdot 10^{-2}$			
Calculated content, at.%			61.7(3) Mo + 38.3(3) C			
Reliability factor			$R_I = 0.056$			

Fig. 17. Fragment of the diffractogram of the Mo–CNT charge after processing in a ball mill, CuK$_\alpha$ radiation. Reflection of the Mo$_3$Fe$_3$C carbide is indicated by '*x*'
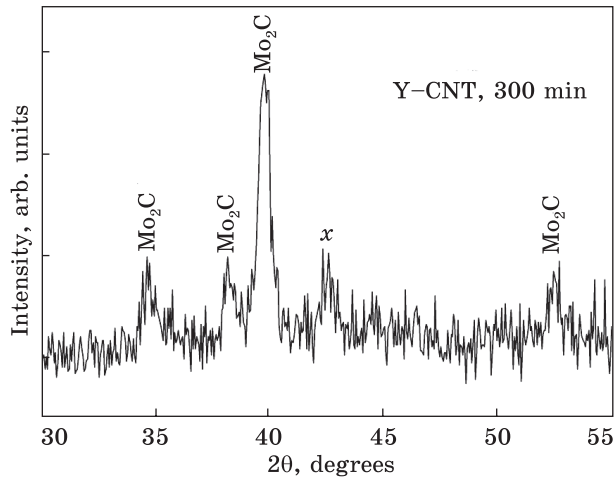
indexing well in a hexagonal lattice with $a = 0.2991(5)$ nm, $c = 0.4744(2)$ nm. That is why the trial model for Mo$_2$C carbide was first made in the frame of the simplest W$_2$C-type structure: *P3m1* space group, Mo atoms are in 2(*d*) (0.333 0.667 0.25) and C atoms are in 1(*a*) (0 0 0). While the refinement of atomic position filling, texture and isotropic temperature factors providing in this structure model framework led to a good agreement between experimental and calculated intensities of reflections at diffraction pattern (the R_B reliability factors is about 0.07), the calculated value of Mo content is equal to 58(1) at.% Mo, which is too small for Mo$_2$C phase. So, the structure model of the ζ-Fe$_2$N-type structure was used as a trial model for Mo$_2$C carbide obtained after 5 hours of processing in a ball mill. It was shown that results of calculation presented in Table 7 characterize the crystal structure correctly [47]. However, the fraction of vacancies in the metal sublattice (≈38 at.% C) is somewhat higher than those inherent to carbon-rich side (≈35 at.% C) of solid solution on the base of the high temperature Mo$_2$C carbide. It is important to note that such a good result was obtained in the case of calculation in the framework of the orthorhombic Mo$_2$C-type structure model, as well. Thus, a more symmetrical ζ-Fe$_2$N-type structure model is preferable in our opinion.

As follows from the phase analysis results, the formation of Mo$_2$C carbide is accompanied with the wear debris (steel vial and balls). Steel (α-Fe, in fact) interacts with MCP products to form a Mo$_3$Fe$_3$C cubic carbide with $a = 1.113(1)$ nm.

The average grain sizes D estimated by the classical Williamson–Hall plots are equal to 5–7 nm as well as average relative deformation of Mo$_2$C lattice ε is equal to 0–0.5%.

Synthesis of the WC Carbide. The W$_2$C carbide was shown to be the main constituent in the test sample selected after 4 hours of milling (Fig. 18). According to Ref. [62] three polymorphic modifications are inherent to this carbide, namely, low temperature 1250–2100 °C W$_2$C
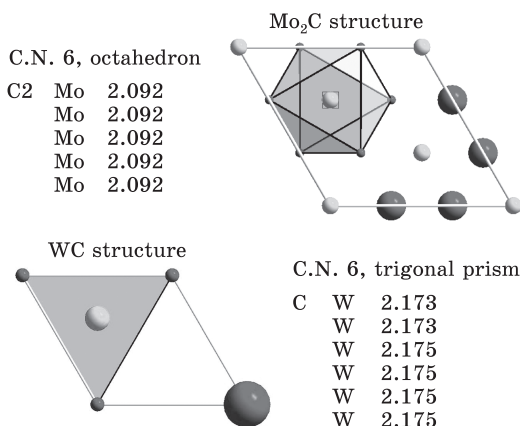
Mo₂C structure

C.N. 6, octahedron

C2	Mo	2.092
	Mo	2.092
	Mo	2.092
	Mo	2.092
	Mo	2.092

WC structure

C.N. 6, trigonal prism

C	W	2.173
	W	2.173
	W	2.175
	W	2.175
	W	2.175
	W	2.175

Fig. 18. Structure mapping of Mo₂C and WC carbides on the *XY* axis (see also this figure online)

with own type structure, high temperature 2100–2400 °C W₂C with Mo₂C-type structure (distorted ζ-Fe₂N-type structure) and high temperature 2400–2780 °C W₂C with ζ-Fe₂N-type structure.

Since the diffraction patterns of phases mentioned above are similar to each other (their structures differ in internal deformation only), each of these type structures was tested as a trial model for determining the crystal structure of W₂C carbide, forming after 4 hours of processing in a ball mill. First calculation was made in the framework of the most simple W₂C type structure ($P3m1$ space group, $a = 0.2984(4)$ nm, $c = 0.4710(4)$ nm): W atoms are placed in $2(d)$ 0.333 0.667 0.25 positions and C atoms are placed in $1(a)$ (0 0 0) positions. Refining of atomic position filling, texture and isotropic temperature factors providing in the framework of this type structure does not lead to a good agreement between experimental and calculated intensities of reflections at the diffraction pattern (R_B reliability factors does not exceed the value of 0.09) as well as to anomalous calculated value of carbide composition (56(1) at.% W). Therefore, further calculations for the W₂C structure were made in the frameworks of the Mo₂C-and ζ-Fe₂N-type structures. Correctness of these calculations was controlled by the reliability factors, which do not exceed the value of 0.05 for each model. That is why a more symmetrical model (ζ-Fe₂N-type structure) was chosen for the W₂C carbide structure (Table 5). As a result, the calculation has revealed that vacancies exist in $6(k)$ position filled with the tungsten atoms. Presence of vacancies in a metal sublattice leads to shift of the W₂C carbide's composition onto ≈35 at.% C, which is inherent to the carbon-rich side of the solid solution on the base of high temperature W₂C modification.

Further processing of the charge in a ball mill leads to gradual W₂C → → WC transformation taking place up to 10 hours of milling (Fig. 19). As follows from the phase analysis results, the formation of WC mono-carbide was accompanied by abrasion of the grinding materials leading to a formation of the cubic W₆Fe₆C carbide with $a = 1.093(1)$ nm. Therefore, along with WC phase the final test sample (10 hours of milling) contains an admixture of W₆Fe₆C phase (marked as '*x*' in

Fig. 19. Fragments of the diffractograms of the W–CNT charge after processing in a ball mill, CuKα radiation. Reflection of the W_6Fe_6C carbide is marked as '*x*'
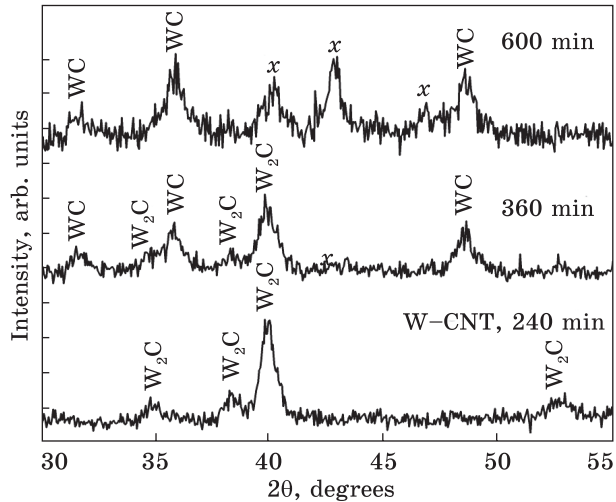

Fig. 19). Crystal structure calculations revealed that WC carbide crystallizes into completely filled structure (own type-structure, space group $P6m2$, $a =$ $= 0.2874(4)$ nm, $c = = 0.2811(5)$ nm): W atoms are located in $1(a)$ (0 0 0), while C atoms are occupy positions in $1(d)$ (0.333 0.667 0.5) ($R_B =$ $= 0.054$). The average grain sizes D of the WC carbide are equal to 4–7 nm. Therefore, the results obtained here have revealed that the reaction milling of the tungsten and CNTs equiatomic mixture results in a stepwise transformation: initial charge $\rightarrow W_2C \rightarrow$ WC. At the first stage (up to 4 hours of processing) the W_2C carbide is formed. It should be noted that a priority of existing the high-temperature W_2C carbide (ζ-Fe_2N-type structure) is expected since it is formed congruently at 2775 °C. At the second stage continuing 6 hours, the WC monocarbide formation is a result of W_2C + CNTs $\rightarrow$ WC transformation. Finally, the WC monocarbide is the main phase constituent of the product obtained after 10 hours of the charge processing in a ball mill.

3.1.3. Carbides of VIIIb Group

Process of the Fe_3C and Co_3C carbides formation have studied on test samples selected stepwise after processing of the initial *Me*–CNT (3:1) charge in a planetary ball mill by the XRD, SEM and TEM methods Initial metals applied for samples preparation are characterized in Table 1.

 Synthesis of the Fe_3C Carbide According to the XRD data the Fe_3C carbide appears for the first time in the test sample selected after 200 min of milling the Fe–CNT charge. In this sample Fe_3C phase coexists with a solid solution on the α-Fe base. A significant amount of the Fe_3C phase was detected in a test sample selected after 300 min of milling (Fig. 20).

 The indexing of the diffraction pattern obtained (Fig. 20) and further calculation of crystal structure refinement indicate that the phase synthesized from the Fe–CNT charge is actually the Fe_3C carbide (Table 8). It should be noted that values of the lattice parameters ob-
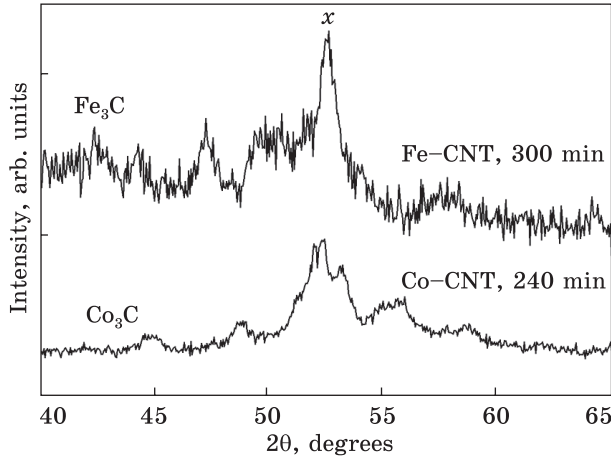
Fig. 20. Fragments of the diffractograms of the *Me*−CNT charge after processing in a ball mill, Co*K*$_\alpha$ radiation. Reflection of the α-Fe is marked as '*x*'

tained here for the Fe$_3$C phase are higher than those for conventional Fe$_3$C carbide, viz.: $a = = 0.5089$ nm, $b = 0.64343$ nm, $c = 0.4526$ nm.

As a result of crystal structure modeling and refinement (Table 8) it was found that mechanochemical processing of the Fe−CNT charge leads to the formation of Fe$_3$C$_{1+x}$ carbide with additional carbon atoms implanting in the Fe$_3$C crystal lattice. An increase in the amount of the carbon atoms leads to a shift in the composition of Fe$_3$C$_{1+x}$ carbide from 25 to 28 at.% C. Taking into account the existence of additional atomic position the crystal structure of the Fe$_3$C$_{1+x}$ carbide could be considered as a new type structure of inorganic compounds. The mapping of this carbide structure of onto the *YZ* plane is presented in Fig. 21.
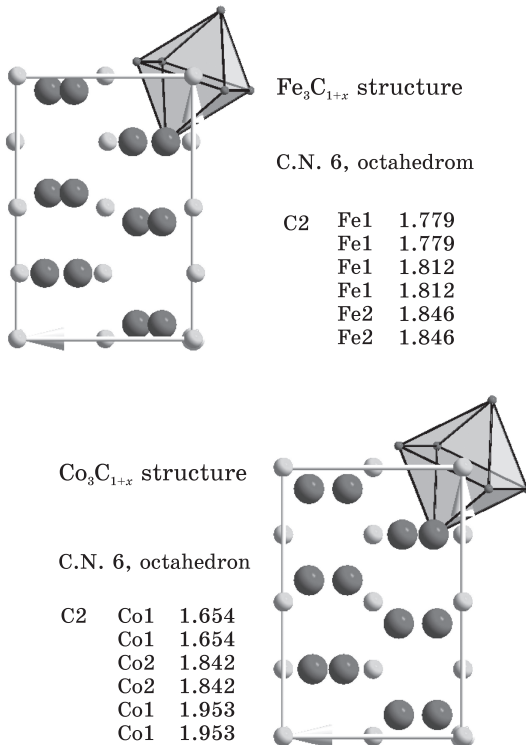

Fe$_3$C$_{1+x}$ structure

C.N. 6, octahedrom

C2	Fe1	1.779
	Fe1	1.779
	Fe1	1.812
	Fe1	1.812
	Fe2	1.846
	Fe2	1.846

Co$_3$C$_{1+x}$ structure

C.N. 6, octahedron

C2	Co1	1.654
	Co1	1.654
	Co2	1.842
	Co2	1.842
	Co1	1.953
	Co1	1.953

Fig. 21. Structure mapping of the Fe$_3$C$_{1+x}$ and Co$_3$C$_{1+x}$ carbides on the *YZ* axis (see also this figure online)

It is known that the crystal structure of the Fe_3C cementite contains four empty equivalent octahedron with the iron atoms in vertexes (α-Fe_6) and with centres in (0 0 0), (0 1/2 0), (1/2 0 1/2), and (1/2 1/2 1/2). They are these empty octahedra, which partially filled with carbon atoms during Fe_3C_{1+x} carbide formation (Fig. 21).

Table 8. **Crystallographic data for Fe_3C and Co_3C carbides formed after 4 hours of processing in a ball mill**

Atom	Site	Site occ.	X	Y	Z
Fe_3C (FeC_{1+x} type structure)					
Fe(1)	8d	1.00(1)	0.198(6)	0.055(4)	0.322(6)
Fe(2)	4c	1.00(1)	0.039(7)	0.25	0.844(6)
C(1)	4c	1.00(1)	0.949(10)	0.25	0.513(12)
C(2)	4a	0.17(4)	0	0	0
Space group			*Pmna*, no. 62		
Lattice parameters, nm			0.5106(9), 0.6774(7), 0.4526(1)		
Independent reflections			62		
Total isotropic factor B, nm^2			$B = 2.15(2) \cdot 10^{-2}$		
Calculated content, at.%			71.9(3) Fe + 28.1(3) C		
Reliability factor			$R_I = 0.075$		
Sintered Fe_3C (FeC_{1+x} type structure)					
Fe(1)	8d	1.00(1)	0.193(4)	0.065(2)	0.348(5)
Fe(2)	4c	1.00(1)	0.059(3)	0.25	0.845(8)
C(1)	4c	1.00(1)	0.966(10)	0.25	0.507(12)
C(2)	4a	0.32(8)	0	0	0
Space group			*Pmna*, no. 62		
Lattice parameters, nm			0.5121(4), 0.6779(5), 0.4550(3)		
Independent reflections			62		
Total isotropic factor B, nm^2			$B = 3.65(2) \cdot 10^{-2}$		
Calculated content, at.%			69.5(3) Fe + 30.5(4) C		
Reliability factor			$R_I = 0.062$		
Co_3C (FeC_{1+x} type structure)					
Co(1)	8d	1.00(1)	0.209(2)	0.080(2)	0.357(4)
Co(2)	4c	1.00(1)	0.074(3)	0.25	0.837(6)
C(1)	4c	1.00(1)	0.050(6)	0.25	0.500(5)
C(2)	4a	1.00(4)	0	0	0
Space group			*Pmna*, no. 62		
Lattice parameters, nm			0.4928(4), 0.6626(5), 0.4404(1)		
Independent reflections			64		
Total isotropic factor B, nm^2			$B = 3.80(2) \cdot 10^{-2}$		
Calculated content, at.%			60.0(4) Co + 40.0(3) C		
Reliability factor			$R_B = 0.067$		

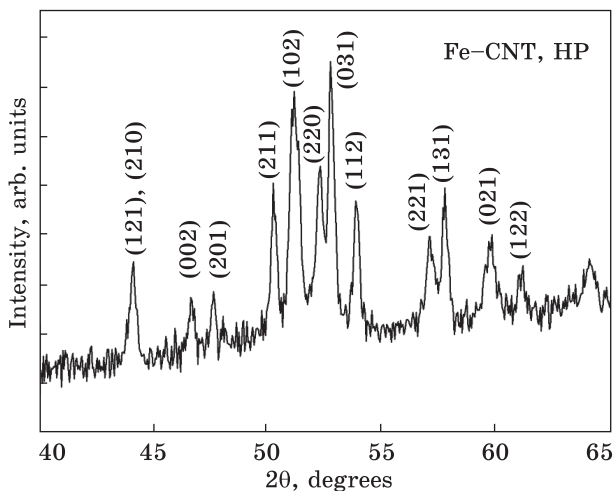*Fig. 22.* Fragment of the diffractogram of the Fe–CNT charge consolidated by HP-HT method, CoKα radiation

From Fig. 20 representing diffraction patterns of the Fe_3C_{1+x} carbide synthesized, it is evident that all diffraction peaks are broadened (calculated crystalline size value is equal to 5–8 nm). This fact prevents to perform crystal structure calculation correctly. That is why the final powder product of synthesis was sintered at high pressure and high temperature (HP-HT method, 8 GPa, 850 °C, holding time of 40 seconds). The toroid type-high pressure apparatus was used to create the pressure (the test powder sample was wrapped into the AlN foil).

The diffraction pattern of the sample consolidated in this way is shown in Fig. 22. In this bulk sample, the calculated values of lattice parameters for the Fe_3C_{1+x} phase are somewhat higher ($a = 0.5121(4)$ nm, $b = 0.6779(5)$ nm, $c = 0.4550(3)$ nm) than those of the initial powder product of MCP (Table 8). The procedure of crystal structure refinement has confirmed a correctness of the model proposed for the Fe_3C_{1+x} carbide and has shown that the solubility of carbon in this phase increases to 30.5 at.% under pressure.

Measurements, which were carried out on the consolidated sample have revealed that average value of the Vickers hardness is equal to 10.4(3) GPa. This hardness value is similar to that for conventional Fe_3C carbide.

Synthesis of the Co₃C Carbide. The x-ray phase analysis of the test samples selected after a certain processing time of the Co–CNT charge in a ball mill, revealed that the Co_3C carbide with a diffraction pattern similar to that for Fe_3C (Fig. 20) appears in test samples after 150 min of milling. The Co_3C phase coexists with the solid solution on the base of hexagonal Co at earlier milling stages. A significant amount of the Co_3C carbide was detected in a test sample selected after 240 min of processing in a ball mill (Fig. 20).

The indexing of the Co_3C diffraction pattern (Fig. 20) and further crystal structure refinement within the framework of both Fe_3C and Fe_3C_{1+x} type structures has revealed that the variant with additional carbon atoms is more preferable (Table 8). It should be noted that if the $4(a)$ position in the Fe_3C_{1+x} carbide structure of is only partially occupied by carbon atoms then the total occupation of the $4(a)$ position is characteristic for Co_3C_{1+x} carbide. Therefore, the composition of this phase shifts from 25 to 40 at.% C. It is also clear that the implantation of the additional carbon atoms to the octahedral pores of the Co_3C structure should cause a significant increase in the value of the lattice parameter. However, the comparison of our data for the Co_3C_{1+x} carbide (Table 8) with the relevant data for conventional Co_3C carbide ($a =$ $= 0.5033$ nm, $b = 0.671$ nm, $c = 0.4483$ nm) certifies the likely decreasing of its lattice parameters at MCP. However, the formation of the Co_3C_{1+x} carbide is accompanied by a substantial internal deformation of the initial Fe_3C type structure (Table 8, Fig. 22). Therefore, since the atomic radius of iron (0.126 nm) is higher than that of cobalt (0.125 nm), the literature data for Co_3C is obviously not correct.

Another metastable carbide, namely, Co_2C (33.3 at.% C) with the $CaCl_2$-type structure, *Pnnm* space group, $a = 0.2910$ nm, $b = 0.4409$ nm, $c = 0.44426$ nm was found earlier in the existence range of the Co_3C_{1+x} carbide (40 at.% C). However, there were no observed traces of this carbide in the synthesis product.

Thus, the Fe_3C_{1+x} and Co_3C_{1+x} carbides have been synthesized by mechanochemical processing and their formation is accompanied by the implantation of additional carbon atoms to the octahedral pores of the Fe_3C type structure.

3.2. Formation Mechanism
of the Transition Metal Carbides at MCP

The eleven carbides of d-transition metals (Table 9) were synthesized by reaction milling of the *Me*–CNT charge. Note that the metals in a form of powder or filings as well as in pieces were used as the initial components of a charge (Table 1).

Test samples selected after a certain time of processing were studied mainly by the XRD method. However, SEM and TEM methods were also applied to study the synthesis of Fe_3C carbide.

Since the carbon nanotubes are x-ray amorphous, the phase composition of the synthesis products was additionally controlled by electron microscopy method. The study has revealed that if the XRD pattern of a test sample selected after 60 min of processing contains α-Fe reflections only, then the electron diffraction pattern of this test sample contains a set of reflections from α-Fe and carbon (Fig. 23, *a*).

Table 9. **Overall characteristics of carbides synthesized by MCP of the *Me*−CNT charge**

Initial metal	Carbon content in a metal	Carbide synthesized	Lattice parameters, nm		
			a	b	c
NaCl modified type structure					
Ti	8(2)	TiC	0.4301(1)	–	–
Zr	7(2)	ZrC	0.4655(1)	–	–
Hf	1	HfC	0.4588(1)	–	–
V	16(2)	VC	0.4156(1)	–	–
Nb	10(2)	NbC	0.4446(1)	–	–
Ta	4(1)	TaC	0.4436(2)	–	–
Y	12(1)	YC_x	0.4894(3)	–	–
ζ-Fe$_2$N type structure					
Mo	5(1)	Mo$_2$C	0.5174(3)	–	0.4744(4)
W	3(1)	W$_2$C	0.5168(3)	–	0.4710(4)
WC type structure					
W	3(1)	WC	0.2874(4)	–	0.2811(5)
Fe$_3$C$_{mod}$ modified type structure					
Fe	9(2)	Fe$_3$C	0.5106(9)	0.6774(7)	0.4526(1)
Co	4(1)	Co$_3$C	0.4928(4)	0.6626(5),	0.4404(1)
Ni	5(1)	–	–	–	–
Cu	2(1)	–	–	–	–

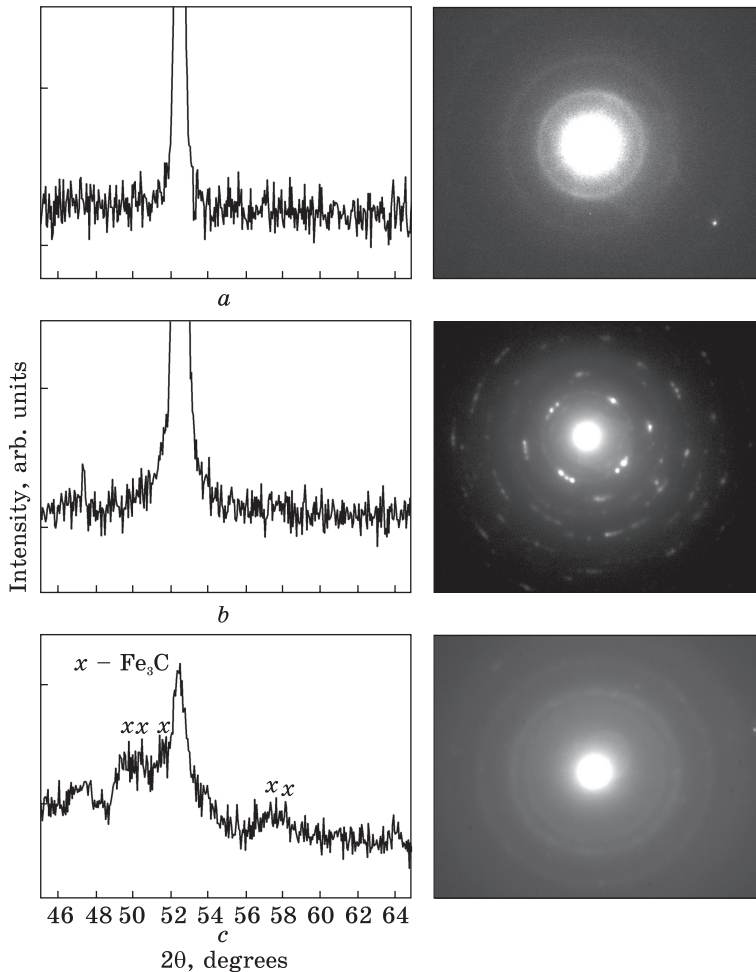| Initial metal	Carbon content in a carbide, at.%		Enthalpy of formation ΔH_f^0, kJ·mole^{-1}
	MCP	Conventional technology	
NaCl modified type structure			
Ti	51.5(5)	48.7	−82.52
Zr	50.6(4)	48.7	−97
Hf	50.0(3)	50.0	−102.4
V	53.2(5)	46.9	−57.8
Nb	50.4(5)	47.7	−66.8
Ta	51.3(4)	48.7	−68.4
Y	?	?	?
ζ-Fe$_2$N type structure			
Mo	38.3(5)	35	−5.25
W	35.1(6)	33	−29
WC type structure			
W	50(3)	50	−29
Fe$_3$C$_{mod}$ modified type structure			
Fe	28(5)	25	1.6
Co	40(4)	25	0.4
Ni	–	–	–
Cu	–	–	–

Fig. 23. Fragment of the diffractogram (CoC_α radiation) and electron diffraction patterns of Fe−CNT samples processed in a ball mill for 60 min (*a*), 150 min (*b*) and 240 min (*c*) [46]

TEM image of this test sample (Fig. 24, *a*) shows that CNT (gray threadlike particles) are moving towards to iron particles (black grains) and partially wrap them. It is known [17] that after 15 min of processing in a high-energy ball mill, carbon nanotubes are crashed onto the onion-like particles, and at the further treatment (up to 60 min) CNT are transformed into amorphous carbon. Therefore, it can be assumed that two processes are realized at the initial stage of the mechanical alloying of the Fe−CNT charge, namely: amorphization of the nanotubes and the destruction of the iron particles. Together, these processes cause the penetration of amorphous carbon along the grain boundaries of iron
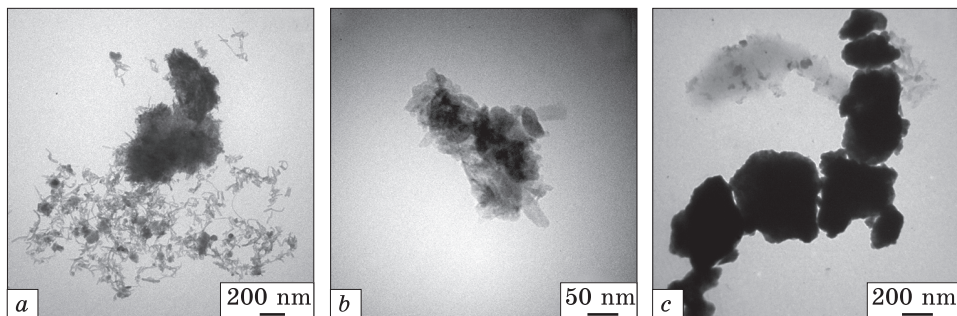
Fig. 24. TEM micrographs of the Fe–CNT samples processed in a ball mill for 60 min (*a*), 150 min (*b*) and 240 min (*c*) [46]

particles, while the destruction of these boundaries increases the contact area between iron and carbon, thereby increasing the reactivity at Fe–CNT interaction.

Further milling of the Fe–CNT charge (longer than 60 min) leads to the gradual formation of the Fe_3C carbide. Although there are no visible reflections of Fe_3C carbide on the diffraction pattern of the test sample obtained after 150 min of milling, its electron diffraction pattern contains separate bright spot-like reflections from Fe_3C carbide additional to the diffraction circles inherent to α-Fe (Fig. 23, *b*). Moreover, there are no individual carbon nanotube pacticles on the TEM image of this sample (Fig. 24, *b*). Obviously, the amorphous carbon interacts with the iron atoms forming a certain nucleation center of the Fe_3C carbide phase on the surface of metal particles (the light-colored inclusions on the surface of the iron particles, Fig. 24, *b*). Besides, at this stage of the milling, the iron grains are significantly deformed resulting in the reducing of the size of their particles.

It is seen (Fig. 24, *c*) that after 240 min of the Fe–CNT charge processing of in a ball mill, the process of intensive exfoliation of the reaction products previously formed on surface of the iron grains begins. TEM image of this sample displays the two types of clusters, namely: dark spots of iron particles and light stains of Fe_3C carbide. In addition, the electron diffraction pattern of this sample shows a superposition of the diffracted reflections of iron and Fe_3C. Moreover, the presence of this carbide could be already detected via x-ray diffraction also (Fig. 23). On this stage, the carbide formation does not completed, but continues mainly with the participation of carbon atoms, which saturated the crystal lattice of iron at the initial stages of milling.

Obviously, that the above processes of the interaction between the iron atoms and carbon nanotubes will also take place at the interaction of CNT with other *d*-metals under the same technological conditions of the *Me*–CNT charge mechanochemical processing.

Thus, at the *first stage* of milling (usually up to 60 min of the charge processing) the total energy of balls collision in a planetary ball mill is spent mainly on the amorphization of carbon nanotubes and on crushing the particles of initial metal along their grain boundaries. Together these processes result in an increase of the number of fine metal particles with a developed surface and enhanced reactivity.

At this stage, amorphous carbon penetrates into the metal lattice, forming an interstitial solid solution due to the lattice and boundary diffusion processes (Tables 1, 2). During diffusion the carbon atoms place predominantly in the deformed octahedral pores of the initial metal lattices with α-Fe (V, Fe, Nb, Mo, Ta, W) and Cu (Ni, Cu) type structures, as well as in the octahedral pores of the rhombic distorted lattice of the initial metals with Mg (Ti, Co, Y, Zr, Hf) type structure (Fig. 8). Thus, at the first stage of milling, the main factor, which regulates the formation of interstitial solid solutions independently on the crystal structure of the initial metal, is the diffusion of the carbon atoms into the lattice of corresponding metal. It was shown that the amount of carbon atoms accumulated by the lattice of metal is well correlated with the value of the activation energy of the carbon diffusion in the corresponding metal (Fig. 25). As a matter of interest, the metal sublattices of all solid solutions become vacant to a varying degree. Moreover, the lattices of metals with Mg type structure become internally deformed.

At the *second stage* of the charge milling (usually processed from 60 to 250 min), process of the carbon atoms penetration into the metal matrix is activated. This stage is also characterized by the initiation of the carbide phase formation on the surface of the initial metal particles. Generally, the milling time, required for complete transformation of initial components to the carbide, correlates with the enthalpy of its
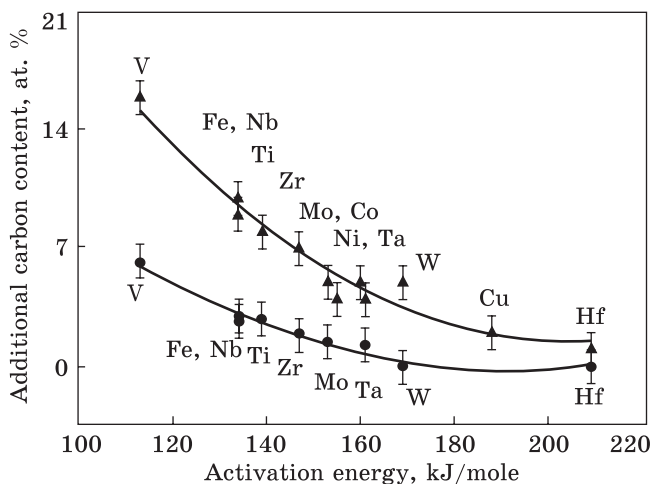

Fig. 25. Dependences of the additional carbon content in metals and carbides on the activation energy of carbon diffusion, where interstitial solid solutions are marked as triangles, carbides are marked as circles
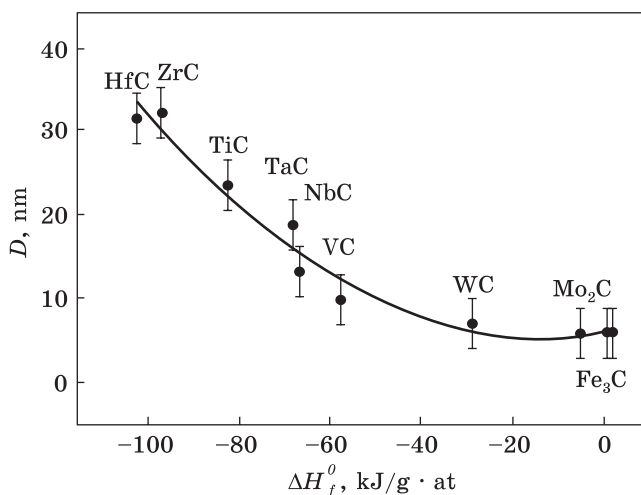
Fig. 26. Dependence of the crystallites size of carbides synthesized at equal conditions on the enthalpy of their formation

formation. Then, if value of the enthalpy of formation for carbide (Table 9, Fig. 26) is lower (more negative), the process of this carbide formation is more favorable thermodynamically. Talking this into account *Me*C monocarbides synthesized could be arranged by the simplicity of their formation in a ball mill (from less to longer treatment time) as HfC → ZrC → TiC → TaC → NbC → VC. Analyzing values of enthalpy of formations listed in Table 9 an approximate time required for a complete formation of these carbides could be estimated.

A detailed study of the crystal structure of MCP phases shows that the excess carbon content is characteristic both for the carbides and for interstitial solid solutions. Moreover, the appearance of this excess of carbon is originated from both the existence of vacancies in metal sublattice of the carbide, and by the implanting of additional carbon atoms to the empty pores (octahedral or cubic) of the crystal structure of carbide. The value of the carbon excess in the structure of the MCP carbide (in relation to the carbon content in the structure of the conventional carbide) correlates with the activation energy of carbon diffusion in the corresponding metal (Fig. 24). That is, the two processes are competing in the formation of carbide phase, namely, diffusion of the carbon atoms to the lattice of initial metal and the formation of a carbide phase from a saturated solid solution obtained.

Finally, at the *third stage* of reaction milling, the formation of carbide is completed. In this case, the carbide particles are exfoliated from the surface of metal particles when reaching the corresponding critical thickness, and subject to milling with a decrease in their crystalline size.

It is interesting, that the enthalpy value of carbide formation is a convenient parameter to analyze the character of crystalline size

variation for MCP carbides. Namely, the higher enthalpy of formation, the faster the carbide is formed.

Thus, XRD study, as well as SEM and TEM examinations of samples selected after a certain time of milling of the *Me*−CNT charge reveals the most probable mechanism for carbide formation. It is clear that the mechanical energy of balls collision is transformed into a heating energy, creating a high-temperature field of local heating. The fact that the high temperature Mo_2C and W_2C carbide modifications were formed in the Mo−CNT and W−CNT systems rather than polymorphic modifications inherent to these phases at temperatures of synthesis (375 K) argues for this assumption. Local temperature heating (creation of the temperature gradients) initiates the process of amorphous carbon diffusion along the boundaries and inside the grains of the initial metal. Enormity of a diffusion flow results from the supersaturation of solid solutions with carbon atoms, which place in the octahedral and cubic pores of metal lattices. Moreover, destruction of this metal lattice due to formation of structural vacancies also takes responsibility for enhanced diffusion value. They are an increase in the reactive surface due to crashing of the metal grains, as well as the presence of local stresses states caused by the diffusion-induced deformation of lattices of the saturated solid solutions that create the conditions for formation of just the carbide phase. Therefore, most likely, the fields of mechanical stress are relaxing in the two main ways, namely, heating and grinding (Fig. 1). Thus, in this work the carbides of *d*-transition metals are formed mainly due to selfsustaining reaction at mechanochemical processing, as previously was shown for TiC in Refs. [57, 58].

4. Interaction in the Metal–Metal′–CNT Ternary Systems

Metal-matrix composites reinforced with ceramic particles (cermet) have found their successful application in chemical, aerospace, automotive, mining, oil and gas industries due to a unique combination of high wear resistance, hardness, strength and corrosion resistance. The success in a synthesis of nanoscale binary transition metal carbides via mechanical alloying of the *Me*−CNT charge prompted us to perform a set of experiments on the synthesis of nanocomposite materials (NCM), where the carbides are formed in the metal matrix directly at milling of the *Me−Me′*−CNT charge (*Me* is the metal matrix, *Me′* is the metal component of a carbide phase). Three compositions in the Fe−Ti−CNT system and two compositions in the Ti−Cu−CNT system were selected as objects of this study. A number of factors, such as relatively low cost of initial metals, carbides synthesis rate, simple procedure of consolidation of the powders milled as well as the expectation of a high strength and plasticity of NCM obtained gives occasion to this choice.

4.1. Fe–Ti–CNT Composites

According to the data for Fe−Ti−C isothermal section [64] there are the three-phase Fe−Fe$_3$C−TiC region bordered by the two-phase Fe-TiC and Fe$_3$C−TiC regions in a solid state. Taking this into account, three compositions were chosen from these regions: 70 wt.% Fe, 24 wt.% Ti and 6 wt.% CNT (56 at.% Fe, 22 at.% Ti and 22 at.% CNT) (*charge 1* for Fe−TiC region); 80 wt.% Fe, 11 wt.% Ti and 9 wt.% CNT (60 at.% Fe, 10 at.% Ti and 30 at.% CNT) (*charge 2* for Fe$_3$C−TiC region); 72 wt.% Fe, 21 wt.% Ti and 7 wt.% CNT) (56 at.% Fe, 9 at.% Ti and 25 at.% CNT) (*charge 3* for Fe−Fe$_3$C−TiC region).

According to the XRD results of the test samples, the formation of TiC carbide begins after 30 min of processing of initial charge in a ball mill. Initial titanium is not detected in the test samples while α-Fe remains their main constituent after 40 min of milling. Further processing of *charge 1* does not lead to a significant change in its phase composition, but the milling of both *charge 2* and *3* is accompanied by the appearance and gradual increase of Fe$_3$C phase, which coexists with the TiC carbide. Finally, according to the results of quantitative phase analysis the test samples selected after 150 min of milling have the following phase composition:

$$\alpha\text{-Fe (75)} + \text{TiC (25)} \ (charge\ 1),$$

$$\text{Fe}_3\text{C (86)} + \text{TiC (14)} \ (charge\ 2),$$

$$\alpha\text{-Fe (34)} + \text{Fe}_3\text{C (33)} + \text{TiC (33)} \ (charge\ 3)$$

(Fig. 27), which practically corresponds to their chosen position on the isothermal section of the Fe−Ti−C system.

It should be noted that the primary formation of the TiC and not Fe$_3$C carbide is not surprising since the free energy of formation of the TiC phase is less than that of the Fe$_3$C phase (Table 9). That is, the formation of TiC carbide is thermodynamically more favorable than that of Fe$_3$C carbide. Therefore, during MCP of the charge the process of TiC formation begins and finishes much earlier than that of Fe$_3$C.

The diffraction peaks on the patterns are significantly broadened (Fig. 27). Therefore, the average values of the grain size D, as well as the average values of microdeformation of the crystal lattice ε have determined for all available phases (α-Fe, Fe$_3$C, and TiC) using the Williamson−Hall plots. It was shown that the crystalline size is equal to 3−10 nm for all these phases.

The milling process of *charge 1* was studied in more details. The analysis of the experimental data obtained shows that the grain size of the TiC carbide formed during MCP is of 3−5 nm. Moreover, for α-Fe phase the dependences of both the grain size and microdeformation of
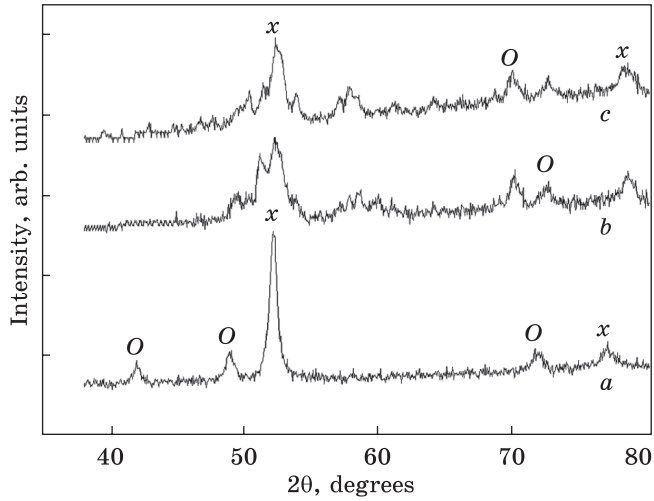
Fig. 27. Fragments of diffractograms for Fe–Ti–CNT samples consolidated via HP-HT method (CoK_α radiation)
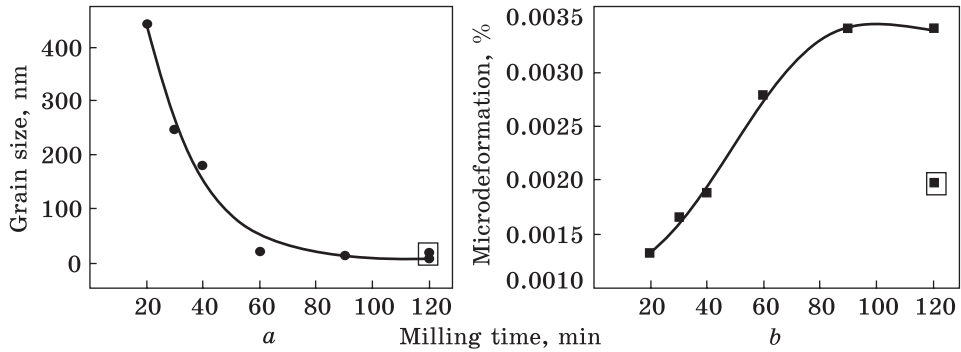

Fig. 28. The processing-time-dependent grain sizes (*a*) and microdeformation (*b*) for the α-Fe phase existing in the Fe–TiC composite (charge *1*)

lattice on the milling time (Fig. 28) can be approximated by exponential curves as

$$D = D_0 \exp(-t/\tau) + D_{\text{fin}},$$

where *t* is the milling time (min), in the case of grain size curve, D_0 and D_{fin} parameters can be interpreted as initial and final size (nm) of crystallites (here, at $\tau \approx 20$ min, $D_0 \approx 1300$ nm, and $D_{\text{fin}} \approx 4$ nm).

In order to study the mechanical properties of the Fe–Ti–CNT composites, the final powder products, selected after 150 min of milling, were consolidated by HP-HT sintering. To ensure the desired sintering parameters (8 GPa, 850 °C, 40 s treatment time), a toroid high pressure cell was used (the powders were wrapped in AlN foil). According to the XRD results, the phase compositions of the samples compacted by HP-HT method are similar to those for powder products (Fig. 28). It is also shown that microdeformations appear in the crystal lattices of TiC
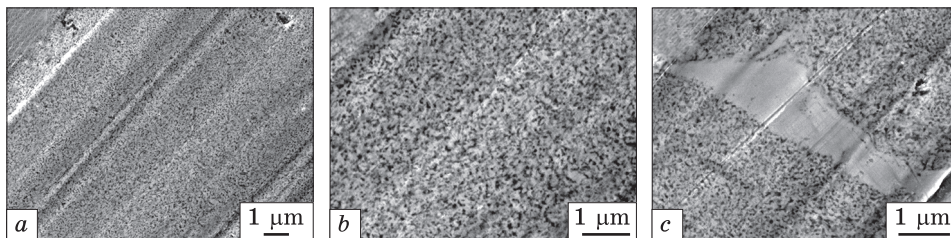
Fig. 29. The SEM micrographs of the compacted Fe−Ti−CNT samples obtained after 120 min of milling charge *1* (*a*), charge *2* (*b*), and charge *3* (*c*) (×2000)
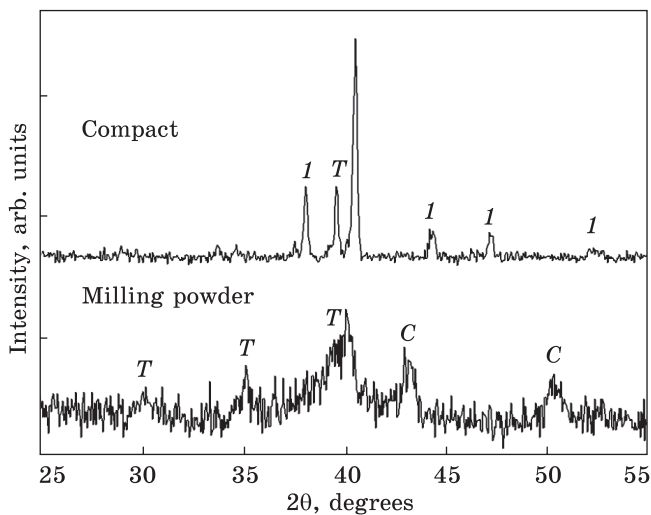

Fig. 30. XRD patterns of the samples obtained by mechanical alloying of the blend (wt.%): Ti : Cu (3 : 1) with 1 vol.% CNT (powder) followed by the sintering of this charge at 980 °C (*T* denotes titanium, *C* — copper, *1* — Ti_2CuC_x)

carbide at high pressure sintering, while those inherent to crystal lattice of α-Fe phase, on the contrary, decreases slightly (stresses in the iron matrix are partially removed). This fact illustrates Fig. 29, which clearly shows the sharpening of peaks presented on the diffraction patterns.

The SEM images obtained show homogeneous phase distribution for the consolidated samples with composition placed on two-phase lines, namely, on Fe−TiC line (*charge 1*) and on Fe_3C−TiC line (*charge 2*) (Fig. 30, *a*, *b*). It was shown that during HP-HT sintering the nanoparticles of the final powders (with a grain size of 4−8 nm) processed in a ball mill are come together in fine-grained (grain size up to 22 nm) solid materials having a quite high compactness. According to the EDS the distribution of the elements in these samples is homogeneous and corresponds to the composition of *charge 1* and *charge 2*, respectively. However, in addition to small inclusions of the carbide phases the sample with composition corresponding to the Fe−Fe_3C−TiC three-phase region (*charge 3*) contains large separate grains of iron (Fig. 30, *c*).

It was naturally to assume that the homogeneous and dense distribution of carbide particles in the iron matrix could lead to an increase

in the mechanical characteristics of nanocomposites obtained. For all three NCMs the Vickers' microhardness has measured on the PMT-3 device at room temperature. Preliminarily all samples have been polished with a diamond paste. The load of 150 g has been applied to the each sample for 15 s. Number of indentations per one sample was 50. Testing of the HP-HT sintered composites reveal the high average Vickers' microhardness values H_V: 11.3(6), 18.3(4), and 14.6(3) GPa for the sample obtained from the *charges 1*, *2*, and *3*, respectively.

4.2. Ti−Cu−CNT Nanocomposites

Two composition were prepared and processed in the Ti−Cu−CNT system, namely, 75 wt.% Ti, 25 wt.% Cu, (79.9 at.% Ti, 20.1 at.% Cu) and 67.7 wt.%. Ti, 33.3 wt.% Cu, (72.7 at.% Ti, 27.3 at.% Cu) [65]. The 1 vol.% CNT was added to both of the mixtures. According to the XRD data, 60 min of the initial charge processing in a ball mill results in the formation of a nanoscale Ti_3Cu intermetallic (a grain size of about 7 nm). However, further processing does not lead to a change in the phase composition of the milling product. Both final products of mechanical synthesis were compacted by cold pressing the powders at room temperature and following sintering at 980 °C. As result of the XRD study, it was found that the phase compositions of the samples compacted in this way are absolutely different from those of the powder products of synthesis.

Thus, it was shown, that the sample with 25 wt.% Cu (20.1 at.% Cu), treated for 60 min in a ball mill and sintered at 980°C, contains a new phase whose diffraction pattern indexing well in a cubic face-cent-red lattice with $a = 1.1514(3)$ nm (this phase is marked as a Ti_2CuC_x carbide in Fig. 21) as well as some addition of the initial titanium [65].

Lattice parameter obtained for Ti_2CuC_x phase and the characteristic positions of its diffraction peaks on the diffraction pattern of this sample give reason to suggest that this phase crystallizes in the Ti_2Ni-type structure with implanting carbon atoms. This assumption is quite natural, as there is well-known Ti_2Cu intermetallic compound, which crystallizes in this type of structure (Ti_2Ni one). That is why the refinement of the crystalline structure of the Ti_2CuC_x carbide was carried out in a model of the Ti_2Ni-type structure with the testing of several variants of the arrangement of implanting carbon atoms. The most suitable trial model, which corresponds to the best correlation between the experimental and calculated values of the intensity of reflections, is given in Table 10. Calculation performed in the framework of this model reveal that the crystal structure of the Ti_2CuC_2 carbide is somewhat defecting in copper atoms (it contains only 30.8 at.% Cu but not 33.3 at.% Cu as usually). Besides, it contains a small amount of carbon atoms implanting therein (only 0.5 at.%). That is, the crystalline
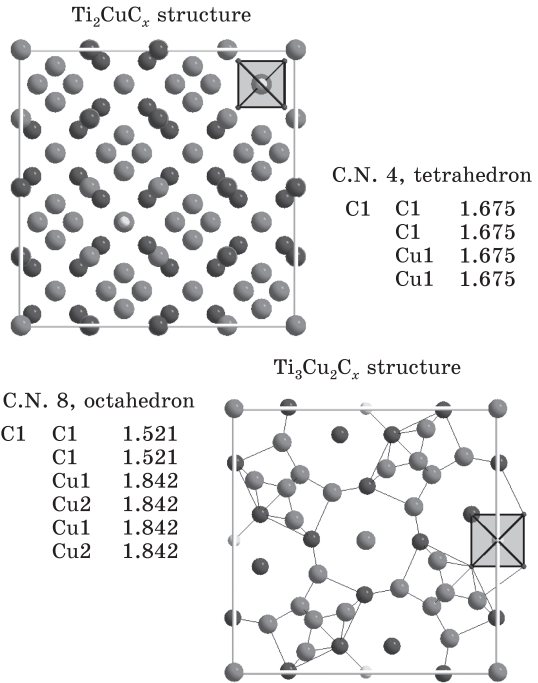
structure of this carbide is very slightly different from the crystalline structure of the Ti_2Cu intermetallic that generates it. The projection of the structure of the Ti_2CuC_x carbide on the XY plane is presented in Fig. 31.

However, during the hot temperature sintering, the nanoscale Ti_3Cu intermetallic existing in the test sample with 27.3 at.% Cu, transforms into a mixture of the above cubic Ti_2CuC_x carbide and the $Ti_3Cu_2C_x$ phase, whose diffraction pattern are indexing well in a tetragonal lattice with $a = 1.1985(2)$ nm, $c = 0.3044(1)$ nm (Fig. 32) [65].

Table 10. **Crystallographic data for triple carbides formed at sintering of the milled Ti−Cu−CNT charge [65]**

Ti$_2$CuC$_x$					
Atom	Site	Site occ.	X	Y	Z
Ti (1)	48f	1.00(1)	0.449(1)	0.125	0.125
Ti (2)	16c	1.00(1)	0	0	0
Cu(1)	32d	0.82(1)	0.209(1)	0.209(1)	0.209(1)
Cu(2)	16e	0.16(1)	0.5	0.5	0.5
C(1)	8a	0.06(1)	0.125	0.125	0.125
Space group			*Fd3m, N* 227		
Lattice parameter a, nm			1.1516(3)		
Independent reflections			34		
Total isotropic factor B, nm²			$B = 2.89(1) \cdot 10^{-2}$		
Calculated content, at.%			68.6 Ti, 30.8 Cu, 0.6 C		
Reliability factor			$R_W = 0.078$		
Ti$_3$Cu$_2$C$_x$					
Атом	Position	Filling	X	Y	Z
Ti(1)	2a	1.00(1)	0	0	0
Ti(2)	8j	0.64(2)	0.128(1)	0.182(1)	0.5
Ti(3)	8j	0.76(2)	0.423(1)	0.228(1)	0
Ti(4)	4g	1.00(1)	0.301(2)	0.199(2)	0
Ti(5)	4h	0.24(1)	0.250(1)	0.250(2)	0.5
Cu(1)	4h	1.00(1)	0.401(1)	0.099(1)	0.5
Cu(2)	4g	0.64(1)	0.099(1)	0.401(1)	0
Cu(3)	8j	0.64(1)	0.995(1)	0.206(1)	0.5
C(1)	4i	0.33(1)	0	0.5	0.25
Space group			$P4/mbm, N$ 127		
Lattice parameters, a, c, nm			1.1986(7), 0.3042(2)		
Independent reflections			80		
Total isotropic factor B, nm²			$B = 3.89(1) \cdot 10^{-2}$		
Calculated content, at.%			58.3 Ti, 37.5 Cu, 4.2 C		
Reliability factor			$R_W = 0.076$		

44

ISSN 1608-1021. Prog. Phys. Met., 2019, Vol. 20, No. 1

Fig. 31. Projection of the carbide $Ti_3Cu_2C_x$ structure onto the *XY* plane, where blue (black), red (grey), and green (light) circles denote titanium, copper, and carbon atoms, respectively (for a better distinguish of different atoms, the reader is referred to the web version of this article)

Ti_2CuC_x structure

C.N. 4, tetrahedron

C1	C1	1.675
	C1	1.675
	Cu1	1.675
	Cu1	1.675

C.N. 8, octahedron

C1	C1	1.521
	C1	1.521
	Cu1	1.842
	Cu2	1.842
	Cu1	1.842
	Cu2	1.842

$Ti_3Cu_2C_x$ structure

Among the phase-analogs suitable for identification of the $Ti_3Cu_2C_x$ phase there is only Ti_3CuN nitride with an unknown crystal structure, which has close values of the tetragonal crystal lattice and similar positions of diffraction peaks. A verifying of several trial models calculated in the $P4/mbm$ space group (precisely this space group has proposed for the Ti_3CuN nitride) led to a fully correct model of the crystal structure of the $Ti_3Cu_2C_x$ carbide (Table 10, Fig. 32). It should be noted that this structure model could be considered as a new, firstly described type structure of the inorganic compounds. According to the data on the calculated composition of this compound it is defecting in both titanium and copper atoms, and it also contains a certain amount of carbon atoms (4.2 at.%),
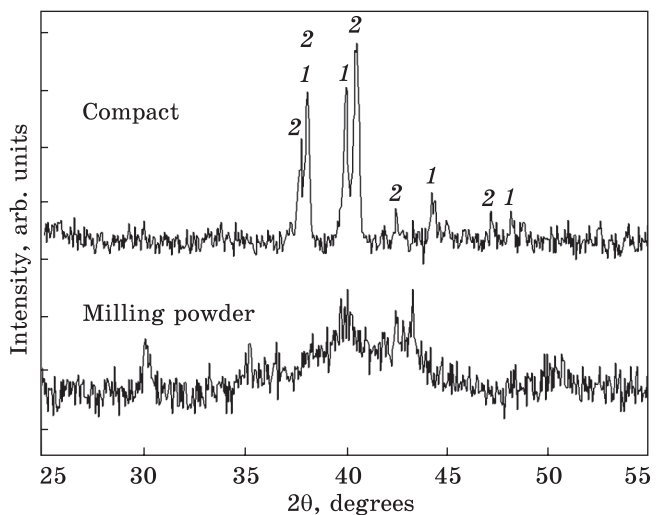

Fig. 32. XRD patterns of the samples obtained by reaction milling of the blend (wt.%) Ti:Cu (2:1) with 1 vol.% of CNT (powder) followed by sintering of this charge at 980 °C (compact): *1* — Ti_2CuC_x, *2* — $Ti_3Cu_2C_x$

which are implanting in the tetrahedral pores of its metal sublattice (Fig. 31).

Thus, the two Ti_2CuC_x and $Ti_3Cu_2C_x$ ternary carbides are formed as a result of heat treatment ($980\,°C$) of MCP products with $20–27$ at.% Cu. The crystal structure of the second carbide is determined for the first time and belongs to a new, previously unknown type structure.

The microhardness measurements, carried out for compacted samples with 20.1 and 27.3 at.% Cu, revealed that these samples are heterogeneous in terms of values obtained, which vary within the $6.9–7.1$ GPa. That is, regardless of the phase composition (availability of both Ti_2CuC_x and $Ti_3Cu_2C_x$ carbides, as well as of other related phases) the average microhardness of the obtained materials is much higher than that for pure titanium (0.97 GPa) and for pure copper (0.37). Thus, an addition to the Ti–Cu mixture with $20–27$ at.% Cu of a small amount of CNT makes a significant effect on the mechanical properties of the nanocomposite materials obtained by compacting the powders treated in a ball mill.

5. Conclusions

A set of experiments on mechanochemical synthesis of d-transition metals binary carbides and composite materials on their basis has performed using multiwalled carbon nanotubes as a carbon component of the charge. As a result, nanoscale powders of the eleven carbides were synthesized, namely, YCx, TiC, ZrC, HfC, VC, NbC, TaC, Mo_2C, WC, Fe_3C, Co_3C. Besides, most of them were synthesized firstly with the use of CNT. In addition, nanocomposite materials of the Fe–Ti–CNT and Ti–Cu–CNT systems were compacted from the powders processed. The nanocomposite materials obtained possess high hardness value, which is provided by the formation of a carbide phase in metal matrix at mechanochemical process directly.

It is shown that at the first stage of mechanochemical processing of the initial powder blend in a ball mill the crystal lattices of metal components of the charge are saturated with the carbon amorphized that leads to formation of interstitial solid solution. At the same time their metallic sublattice, on the contrary, becomes defecting on metals. Both of these factors cause the supersaturation of solid solutions based on the initial metals. Moreover, the amount of excess carbon (in relation to its solubility under thermodynamically equilibrium conditions) correlates well with the activation energy of carbon diffusion into the lattice of the corresponding metal.

On the second stage the crystal structures of the binary carbides, which are formed on the basis of distorted lattices of interstitial solid

solution, are usually modified and characterized by additional carbon atoms, which are placed in the pores of their initial structures (NaCl and Fe_3C type).

The complex of XRD, SEM and TEM data have revealed that the *d*-transition metal carbides studied in this work at MCP are formed mainly due to a self-sustaining reaction.

Efficiency of the carbon nanotubes application for manufacturing of nanocomposite materials with advanced properties has shown. Mechanical characteristics of these materials are regulated by the nanoscale metal matrix and carbide phase, by the high density and by structural features of their constituents (usually supersaturated with additional carbon).

Generally, the mechanochemical method can be very effective for the synthesis of multicomponent carbides (substitutional solid solutions), which cannot be obtained in any other ways. Since the duration of the incubation period (the time before the formation of the carbide phase begins) correlates with the enthalpy of formation of this carbide, the criterion for formation of such mutual solid solutions could be the similarity of their crystal structures and the proximity of the energies of their formations.

REFERENCES

1. P. Balaz, *Acta Metalurgica Slovaca*, No. 4: 23 (2001).
2. V. Boldyrev, *Khimiya v Interesakh Ustoichivogo Razvitiya*, **10**, Nos. 1–2: 3, (2002) (in Russian).
3. M. Carry-Lea, *Am. J. Sci.*, **141**: 259 (1891).
4. E.P. Elsukov, I.V. Povstugar, A.L. Ul'yanov, and G.A. Dorofeev, *Fiz. Met. Metalloved.*, **101**, No. 2: 193 (2006) (in Russian).
5. A.C. Damask and G.J. Dienes, *Point Defects in Metals* (Gordon and Breach, 1st edition: 1963).
6. A.M. Shalaev, *Radiatsionno-Stimulirovannaya Diffuziya v Metallakh* [Radiation-Induced Diffusion in Metals] (Moscow: Atomizdat: 1972) (in Russian).
7. L.N. Larikov and V.M. Kal'chenko, *Mekhanizm Vliyaniya Fazovykh Prevrashcheniy na Diffuziyu. Diffuziya v Metallah i Splavah* [Mechanisms of Influence of the Phase Transformations on Diffusion. Diffusion in Metals] (Tula: 1968) (in Russian).
8. S.D. Gercriken and V.M. Fal'chenko, *Voprosy Fiziki Metallov i Metallovedeniya*, No. 16: 153 (1962) (in Russian).
9. B.S. Bokshtejn, S.Z. Bokshtein, and A.A. Zhuhovickiy, *Termodinamika i Kinetika Diffuzii v Tverdykh Telakh* [Thermodynamics and Kinetics of Diffusion in Solids] (Moscow: Metallurgiya: 1974) (in Russian).

10. R.W. Baluffi and A.J. Ruoff, *J. Appl. Phys.*, **34**, No. 6: 1634 (1963). https://doi.org/10.1063/1.1702647
11. A.J. Ruoff and R.W. Baluffi, *J. Appl. Phys.*, **34**, No. 7: 1848 (1963). https://doi.org/10.1063/1.172969
12. V.M. Lomer, *Vakansii i Tochechnye Defekty* [Vacancies and Point Defects] (Moscow: Metallurgizdat: 1961) (in Russian).
13. Yu.P. Romashkin, *Fiz. Tverd. Tela*, **11**, No. 12: 1059 (1960) (in Russian).
14. V.V. Neverov, V.N. Burov, and A.I. Korotkov, *Fiz. Met. Metalloved.*, **48**, No. 5: 978 (1978) (in Russian).
15. J.S. Benjamin, *Sci. Am.*, **234**, No. 5: 40 (1976).
16. J.S. Benjamin, *Mat. Sci. Forum*, **88–90**: 1 (1992). https://doi.org/10.4028/www.scientific.net/MSF.88-90.1
17. P.H. Shingu, *Mechanical Alloying*, **88–90** (Zurich: Trans Tech Publ.: 1992). https://doi.org/10.4028/www.scientific.net/MSF.88-90
18. V.V. Boldyrev, *Eksperimental'nye Metody v Mekhanokhimii Tverdykh Neorganicheskikh Veshchestv* [Experimental Methods in Mechanochemistry of Solid Inorganics] (Novosibirsk: Nauka. Siberian branch: 1983) (in Russian).
19. V.V. Boldyrev, *Kinetika i Kataliz*, **13**, 1411 (1972) (in Russian).
20. V. Boldyrev and G. Heinicke, *Z. Chem. B*, **19**: 356 (1975).
21. N.Z. Lyahov and V.V. Boldyrev, *Izv. SO AN SSSR. Ser. Khim.*, **5**: 8 (1985) (in Russian).
22. N.S. Lyakhov, *Proc. Second Japan–Soviet Symposium on Mechanochemistry* (Eds. G. Jimbo, M. Senna, and Y. Kuwohara) (Tokyo: Publishing Society Powder Technology: 1988), p. 59.
23. Yu.T. Pavlukhin, Ya.Ya. Medikov, and V.V, Boldyrev, *Izv. SO AN SSSR, Ser. Khim.*, **4**: 11 (1981) (in Russian).
24. Y.T. Pavlukhin, Ya.Ya. Medikov, and V.V. Boldyrev, *J. Solid State Chem.*, **53**, No. 2: 155 (1984). https://doi.org/10.1016/0022-4596(84)90089-6
25. Yu.T. Pavlukhin, Ya.Ya. Medikov, and V.V. Boldyrev, *Rev. Solid State Sci.*, **2**: 603 (1988).
26. H. Heegn, *Proc. First Int. Conf. Mechanochemistry* (Cambridge: Cambridge Intersci. Publ.: 1993), p. 11.
27. R.B. Schwarz and C.C. Koch, *Appl. Phys. Lett.*, **49**, No. 3: 146 (1986). https://doi.org/10.1063/1.97206
28. D.R. Maurice and T. Courtney, *Metall. and Mat. Trans. A*, **21**: 289 (1990). https://doi.org/10.1007/BF02782409
29. V.V. Boldyrev, V.R. Regel', O.F, Pozdnyakov, F.H. Urukaev, and B.Ya. Byl'skij, *Dokl. AN SSSR*, **221**: 634 (1975) (in Russian).
30. F.H. Urukaev, V.V. Boldyrev, O.F, Pozdnyakov, and V.R. Regel', *Kinetika i Kataliz*, **18**, 350 (1977) (in Russian).
31. E.L. Goldberg, S.V. Pavlov, *Proc. Second World Congress on Particle Technology* (Ed. G. Jimbo) (Kyoto: Japan Society Technology: 1990), p. 507.
32. V.V. Boldyrev, S.V. Pavlov, and E.L. Goldberg, *Intern. J. Miner. Proc.*, **44–45**: 181 (1996).
33. C.C. Koch, *Mater. Trans., JIM*, **36**, No. 2: 85 (1995). https://doi.org/10.2320/matertrans1989.36.85
34. C. Suryanarayana, *Progress Mater. Sci.*, **46**, Nos. 1–2: 1 (2001). https://doi.org/10.1016/S0079-6425(99)00010-9
35. C. Suryanarayana and N. Al-Aqeeli, *Progress Mater. Sci.*, **58**, No. 4: 383 (2012). https://doi.org/10.1016/j.pmatsci.2012.10.001
36. T.F. Grigorieva, A.P. Barinova, and N.Z. Lyakhov, *Russ. Chem. Rev.*, **70**: 45 (2001). https://doi.org/10.1070/RC2001v070n01ABEH000598

37. P.Y. Butyagin, *Russian Scientiéc Review. Sect. B: Chemistry Reviews*, **2**, Pt. 2: 89 (London: Harwood Academic Publ.: 1998).

38. R. Schwarz, *Mater. Sci. Forum*, **269–272**: 665 (1998). https://doi.org/10.4028/www.scientific.net/MSF.269-272.665

39. V.K. Pecharsky and P.Y. Zavalij, *Fundamentals of Powder Diffraction and Structural Characterization of Materials* (New-York: Springer: 2009). https://doi.org/10.1007/978-0-387-09579-0

40. M. Dashevskyi, O. Boshko, O. Nakonechna, and N. Belyavina, *Metallofiz. Noveishie Tekhnol.*, **39** No. 4: 541 (2017). https://doi.org/10.15407/mfint.39.04.0541

41. G.K. Williamson and W.H. Hall, *Acta Met.*, **1**, No. 1: 22 (1953). https://doi.org/10.1016/0001-6160(53)90006-6

42. S. Iijima, *Nature*, **354**: 56 (1991). https://doi.org/10.1038/354056a0

43. X. Long, Y. Bai, M. Algarni, Y. Choi, and Q. Chen, *Mat. Sci. Eng. A*, **645**: 347 (2015). https://doi.org/10.1016/j.msea.2015.08.012

44. R.A. Andrievskiy and A.V. Ragulya, *Nanostrukturnye Materialy* [Nanostructured Materials] (Moscow: Academiya: 2005) (in Russian).

45. O. Boshko, O. Nakonechna, M. Dashevsky, K. Ivanenko, N. Belyavina, and S. Revo, *Adv. Powder Technol.*, **27**, No. 4: 1101 (2016). https://doi.org/10.1016/j.apt.2016.03.019

46. O. Boshko, O. Nakonechna, N. Belyavina, M. Dashevsky, S. Revo, *Adv. Powder Technol.*, **28**, No. 3: 964 (2017). https://doi.org/10.1016/j.apt.2016.12.026

47. O. Nakonechna, M. Dashevskyi, and N. Belyavina, *Metallofiz. Noveishie Tekhnol.*, **40**, No. 5: 637 (2018). https://doi.org/10.15407/mfint.40.05.0637

48. P. Matteazzi and G. Le Caër, *J. Am. Ceram. Soc.*, **74**, No. 6: 1382 (1991). https://doi.org/10.1111/j.1151-2916.1991.tb04116.x

49. A. Teresiak and H. Kubsch, *Nanostruct. Mater.*, **6**, Nos. 5–8: 671 (1995). https://doi.org/10.1016/0965-9773(95)00147-6

50. Q. Yuan, Y. Zheng, and H. Yu, *Int. J. Refract. Met. Hard Mater.*, **27**, No. 4: 696 (2009). https://doi.org/10.1016/j.ijrmhm.2008.11.003

51. H. Jia, Z. Zhang, Z. Qi, G. Liu, and X. Bian, *J. Alloys Compd.*, **472**, Nos. 1–2: 97 (2009). https://doi.org/10.1016/j.jallcom.2008.04.070

52. B. Ghosh and S.K. Pradhan, *Mater. Chem. Phys.*, **120**, Nos. 2–3: 537 (2010). https://doi.org/10.1016/j.matchemphys.2009.11.048

53. C.J. Lu and Z.Q. Li, *J. Alloys Compd.*, **395**, Nos. 1–2: 88 (2005). https://doi.org/10.1016/j.jallcom.2004.11.046

54. N.J. Calos, J.S. Forrester, and G.B. Schaffer, *J. Solid State Chem.*, **158**, No. 2: 268 (2001). https://doi.org/10.1006/jssc.2001.9107

55. L. Takacs, *J. Solid State Chem.*, **125**, No. 1: 75 (1996). https://doi.org/10.1006/jssc.1996.0267

56. B.H. Lohse, A. Calka, and D. Wexler, *J. Alloys Compd.*, **434–435**: 405 (2007). https://doi.org/10.1016/j.jallcom.2006.08.216

57. N.Q. Wu, G.X. Wang, J.M. Wu, Z.Z. Li, and M.Y. Yuan, *Int. J. Refract. Met. Hard Mater.*, **15**, Nos. 5–6: 289 (1997). https://doi.org/10.1016/S0263-4368(97)87504-X

58. X.K. Zhu, K.Y. Zhao, B.C. Cheng, Q.S. Lin, X.Q. Zhang, T.L. Chen, and Y.S. Su, *Mater. Sci. Eng. C*, **16**, Nos. 1–2: 103 (2001). https://doi.org/10.1016/S0928-4931(01)00283-1

59. E.P. Elsukov and G.A. Dorofeev, *Khimiya v Interesakh Ustoichivogo Razvitiya*, **10**: 59 (2002) (in Russian).

60. E.P. Elsukov, G.A, Dorofeev, and V.V. Boldyrev, *Khimiya v Interesakh Ustoichivogo Razvitiya*, **10**: 53 (2002) (in Russian).

61. E.P. Yelsukov, G.A. Dorofeev, V.A. Barinov, T.F. Grigorieva, and V.V. Boldyrev, *Mater. Sci. Forum*, **269–272**: 151 (1998). https://doi.org/10.4028/www.scientific.net/MSF.269-272.151

62. N.P. Lyakishev, *Fazovye Diagrammy Binarnyh Metallicheskikh Sistem* [Phase Diagrams of Binary Metallic Systems] (Moscow: Mashinostroeniye: 1996) (in Russian).

63. Y.B. Li, B.Q. Wei, J. Liang, Q.Yu, and D.H. Wu, *Carbon*, **37**, No. 3: 493 (1999). https://doi.org/10.1016/S0008-6223(98)00218-8

64. V. Raghavan, *J. Phase Equilib.*, **24**, No. 1: 62 (2003). https://doi.org/10.1007/s11669-003-0010-8

65. O.I. Nakonechna, N.N. Belyavina, M.M. Dashevskyi, K.O. Ivanenko, and S.L. Revo, *Phys. Chem. Solid State*, **19**, No. 2: 179 (2018). https://doi.org/10.15330/pcss.19.2.179-185

O.I. Наконечна[1], М.М. Дашевський[1],
O.I. Бошко[2], В.В. Заводянний[3], Н.М. Білявина[1]

[1] Київський національний університет імені Тараса Шевченка,
  просп. Глушкова, 4, 03022 Київ, Україна

[2] Інститут металофізики ім. Г.В. Курдюмова НАН України,
  бульв. Академіка Вернадського, 36, 03142 Київ, Україна

[3] Херсонський державний аграрний університет,
  вул. Стрітенська, 23, 73006 Херсон, Україна

ВПЛИВ ВУГЛЕЦЕВИХ НАНОТРУБОК
НА МЕХАНОХІМІЧНИЙ СИНТЕЗ НАНОПОРОШКІВ
КАРБІДІВ *d*-МЕТАЛІВ І НАНОКОМПОЗИТІВ НА ЇХ ОСНОВІ

Механохімічним методом у високоенергетичному планетарному кульовому млині з шихти, що містить вуглецеві нанотрубки, синтезовано нанорозмірні моно-(порошки) та подвійні (компактовані нанокомпозити) карбіди *d*-перехідних металів. Розглянуто вплив багатошарових вуглецевих нанотрубок на механохімічний синтез одержаних матеріалів. З'ясовано особливості механізму формування карбідів перехідних металів у процесі механохімічного синтезу. Зокрема, показано, що на першому етапі синтезу (до 60 хв оброблення шихти) має місце аморфізація вуглецевих нанотрубок і подрібнення частинок вихідного металу по межах зерен. Надалі аморфізований вуглець потрапляє всередину ґратниці металу, утворюючи твердий розчин втілення, внаслідок чого металеві підґратниці набувають дефектности. На другому етапі синтезу (від 60 до 250 хв розмелювання) процес втілення атомів Карбону в металічну матрицю пришвидшується та починається формування карбідних фаз на поверхні частинок вихідного металу. Третій етап синтезу завершує формування карбіду. Встановлено, що час розмелювання, потрібний для повного перетворення вихідних компонентів у карбід, корелює з ентальпією його утворення, а поля механічних напружень релаксують за двома основними напрямами: нагрівання та подрібнення. Виявлено, що досліджені в даній роботі карбіди *d*-перехідних металів під час механохімічного синтезу формуються в основному за рахунок самопідтримуваної реакції. Показано ефективність використання вуглецевих нанотрубок при створенні нанокомпозиційних матеріалів з поліпшеними функціональними характеристиками. Встановлено, що механохі-

мічний метод є ефективним для синтезу багатокомпонентних карбідів (твердих розчинів заміщення), одержати які іншими способами майже неможливо.

Ключові слова: механохімічний синтез, вуглецева нанотрубка, карбід, твердий розчин, рентгенівська дифракція, електронна мікроскопія.

О.И. Наконечная[1], Н.Н. Дашевский[1],
О.И. Бошко[2], В.В. Заводянный[3], Н.Н. Белявина[1]

[1] Киевский национальный университет имени Тараса Шевченко,
  просп. Глушкова, 4, 03022 Киев, Украина
[2] Институт металлофизики им. Г.В. Курдюмова НАН Украины,
  бульв. Академика Вернадского, 36, 03142 Киев, Украина
[3] Херсонский государственный аграрный университет,
  ул. Стретенская, 23, 73006 Херсон, Украина

ВЛИЯНИЕ УГЛЕРОДНЫХ НАНОТРУБОК НА МЕХАНОХИМИЧЕСКИЙ СИНТЕЗ НАНОПОРОШКОВ КАРБИДОВ d-МЕТАЛЛОВ И НАНОКОМПОЗИТОВ НА ИХ ОСНОВЕ

Механохимическим методом в высокоэнергетической планетарной шаровой мельнице из шихты, содержащей углеродные нанотрубки, синтезированы наноразмерные моно- (порошки) и двойные (компактированные нанокомпозиты) карбиды d-переходных металлов. Рассмотрено влияние многослойных углеродных нанотрубок на механохимический синтез полученных материалов. Выяснены особенности механизма формирования карбидов переходных металлов в процессе механохимического синтеза. В частности, показано, что на первом этапе синтеза (до 60 мин обработки шихты) имеет место аморфизация углеродных нанотрубок и измельчение частиц исходного металла по границам зёрен. В дальнейшем аморфизированный углерод попадает внутрь решётки металла, образуя твёрдый раствор внедрения, в результате чего металлическая подрешётка становится дефектной. На втором этапе синтеза (от 60 до 250 мин размола) процесс внедрения атомов углерода в металлическую матрицу ускоряется и начинается формирование карбидных фаз на поверхности частиц исходного металла. Третий этап синтеза завершает формирование карбида. Установлено, что время размола, необходимое для полного преобразования исходных компонентов в карбид, коррелирует с энтальпией его образования, а поля механических напряжений релаксируют по двум основным каналам: нагрев и измельчение. Обнаружено, что исследованные в данной работе карбиды d-переходных металлов при механохимическом синтезе формируются в основном за счёт самоподдерживающейся реакции. Показана эффективность использования углеродных нанотрубок при создании нанокомпозиционных материалов с улучшенными функциональными характеристиками. Установлено, что механохимический метод является эффективным для синтеза многокомпонентных карбидов (твёрдых растворов замещения), получить которые другими способами практически невозможно.

Ключевые слова: механохимический синтез, углеродная нанотрубка, карбид, твердый раствор, рентгеновская дифракция, электронная микроскопия.